Accepted Manuscript

A grain boundary formulation for crystal plasticity

I. Benedetti, V. Gulizzi, V. Mallardo

Please cite this article as: Benedetti, I., Gulizzi, V., Mallardo, V., A grain boundary formulation for crystal plasticity, *International Journal of Plasticity* (2016), doi: 10.1016/j.ijplas.2016.04.010.

A grain boundary formulation for crystal plasticity

I. Benedetti*, V. Gulizzi

Dipartimento di Ingegneria Civile, Ambientale, Aerospaziale, dei Materiali - DICAM
Università degli Studi di Palermo, Viale delle Scienze, 90128, Palermo, Italy

V. Mallardo

Dipartimento di Architettura
Università degli Studi di Ferrara, Via della Ghiara 36, 44121, Ferrara, Italy

Abstract

A three-dimensional grain-boundary formulation for *small strains* crystal plasticity is presented for the first time. The method is developed and implemented for both single grains and polycrystalline aggregates and it is based on the use of a suitable set of boundary integral equations for modelling the individual grains, which are represented as *anisotropic* elasto-plastic domains. In the boundary integral framework, crystal plasticity is modelled resorting to an *initial strains* approach and specific aspects, related to the integration of strongly singular volume integrals in the anisotropic elasto-plastic grain-boundary equations, are discussed and suitably addressed for the first time. In the poly-crystalline case, Voronoi-type micro-morphologies are discretised using robust non-structured *boundary* and *volume* meshes. A general grain-boundary incre-mental/iterative algorithm, embedding rate-dependent flow and hardening rules for crystal plasticity, is developed and discussed. The method has been assessed through several numerical simulations, for both single and polycrystalline ag-gregates, which confirm its robustness and accuracy and suggest directions for further developments. The key feature of the formulation is the expression of the micro-mechanical problem in terms of grain-boundary variables only, namely

---

*Corresponding author
  Email addresses: `ivano.benedetti@unipa.it` (I. Benedetti),
`vincenzo.gulizzi@unipa.it` (V. Gulizzi), `vincenzo.mallardo@unife.it` (V. Mallardo)

inter-granular displacements and tractions, which results in a reduction of the total number of degrees of freedom, which may be appealing in a multi-scale framework.

1. Introduction

Polycrystalline materials are widely used in engineering applications. In recent years, due to the advancements in microstructural materials characterization and the wider affordability of High Performance Computing (HPC),
5 much interest has been focused on microstructural modeling of materials, in which an increasing number of microstructural features and details are included in the material representation, in an attempt to capture the origin of several macroscopic effective material behaviours. The interest in microstructural modelling has also been motivated by the increasing use of micro-mechanical devices
10 (MEMS, stents, etc.), in which the application scale is often comparable with the grains' size. In particular, three-dimensional computational modeling is today a very active research area [1].

One of the main deformation mechanisms active in crystals, at the grain level, is plastic slip over well defined crystallographic planes. The phenomenon, known
15 as crystal plasticity, is characterised by its inherent anisotropy, induced by the structure of the crystalline lattice itself. Several numerical and computational methods have been proposed in the literature for the analysis of plasticity in single crystals and crystal aggregates. A very complete review of Crystal Plasticity Finite Element Methods (CPFEMs) can be found in [2], where a wide range
20 of continuum-based techniques and contributions, with applications in fields as diverse as texture evolution, creep, nano indentation, forming and others, is discussed. A detailed comparison among three different theoretical frameworks, i.e. conventional continuum plasticity, discrete dislocation plasticity and nonlocal plasticity, is reported by Needleman [3], who strongly underlines the

importance of computational studies.

Several studies have been devoted to the modelling of plastic slip in single crystals. Both rate–dependent (RD) [4, 5, 6] and rate–independent (RI) [7] models have been proposed and compared [8]. Much research has also been focused on the development of crystal plasticity models for *polycrystalline* aggregates [2]. Several 3D CPFEMs were initially developed to assess texture development in polycrystals. In several studies, the aggregate was represented with simple morphologies and coarse meshes, with individual grains often modelled by a single finite element. Despite such approximations, the models were quite accurate in predicting texture evolution. In [9] a Taylor-type polycrystal plasticity model was tested in large strain reverse torsion tests, with the different slip hardening laws presented by Asaro & Needleman [10], by Harren *et al.* [11], by Bassani & Wu [12] and by Kalidindi *et al.* [13].

Both 2D [14] and fully 3D [15] polycrystalline models, with the explicit representation of individual grains, have been developed, using a rate–dependent CPFEM formulations. Quilici and Cailletaud [16] developed a CPFEM framework that was subsequently used for the analysis of stress/strain fields within 3D polycrystalline aggregates in the small strains regime [17, 18]. Voronoi tessellations have been used to represent the microstructure and a visco-plastic crystallographic constitutive model, with isotropic and kinematic hardening, was employed. Aggregates up to 200 grains were analyzed and the FETI (Finite Element Tearing and Interconnecting) method [19] was employed, in conjunction with High Performance Computing, to tackle the high computational requirements of 3D computations. The same strategy was later employed by Diard *et al.*[20], who analyzed micro-plasticity in hexagonal close-packed materials, with *as realistic as possible* microstructures. Sarma and Radhakrishnan [21] applied CPFEM for studying the hot deformation of grains in polycrystalline aluminum. They report that, due to the time-consuming nature of such simulations, it was possible to consider only a limited number of specially constructed microstructures. Zeghadi *et al.*[22] performed, in a CPFEM framework, a statistical analysis on several different 3D morphologies generated starting from

3

the same 2D surface. Aggregates with around 40 grains were considered and the plastic strain fields over the reference 2D surface, induced by different internal 3D morphologies of the assessed specimen, were investigated. It was found that large fluctuations in the equivalent plastic slip level are induced by different internal 3D morphologies, under the same external loading conditions, thus advocating the need of fully 3D studies over simplified pseudo 3D (or 2D columnar) studies.

Similar studies, focused on the comparison between experimental and computational results, with the aim of identifying possible sources of error and better calibrating microstructural constitutive parameters were performed by Héripré et al.[23], Musienko et al.[24], Zhang et al. [25] and Pinna et al.[26]. Musienko et al.[24] analyzed an experimentally reconstructed copper specimen with approximately 100 grains. CPFEM was used and the results of fully 3D and columnar 2D (pseudo-3D) simulations were compared, to assess the bias introduced by the simplified morphologies. It was found that the computational results of the fully 3D mesh were in good agreement with the experimental data, while only some traces of the experimental behaviour were retained in the extended 2D simulations. Zhang et al. [25] compared, in terms of stress-strain curves and lattice reorientation, the experimental results obtained from a tensile test of a Ti-5Al-2.5Sn specimen with those obtained from numerical CPFEM simulations using 2D columnar and 3D microstructures. The stress-strain curve was used to calibrate the parameters of the crystal plasticity constitutive model. Using the lattice reorientation maps, the authors showed that fully 3D microstructures better reproduced the experimental observations with respect to the pseudo 3D microstructures. Pinna et al. [26] simulated the deformation of a FCC aluminium alloy AA5052 at high temperatures using a structured mesh where each cubic volume element had its own crystallographic orientation, and a Fe-30wt%Ni alloy using a two dimensional mesh with plane strain assumption. Besides the qualitative agreement between the numerical results and the experimental measurements in terms of stress-strain curves, the authors reported the limitations of simplified CPFEM models to capture the intra-granular strain

4

distribution and suggested the use of fully three-dimensional models.

Barbe and Quey [27] presented a CPFEM model for 3D polycrystalline microstructures, including polycrystal-to-polycrystal diffusive transformations. Schneider *et al.* [28, 29] investigated the mechanical behavior of αFe-Cu composites under large plastic deformations in simple tension and compression, using 3D FEM simulations (ABAQUS) with an elasto-visco-plastic material model. Crack initiation and evolution in polycrystalline aggregates is addressed in [30], where the cohesive-zone type contact is implemented in a CPFEM framework employing Bassani-Wu hardening laws. In [31], a comparison between the self-consistent, finite element and spectral methods is carried out in the context of homogenization of polycrystalline aggregates with an elastic-viscoplastic behaviour. Zhang *et al.* [32] studied the anisotropic mechanical response of a rolled AA1050 aluminium plate with respect to the loading direction using five different crystal plasticity models, showing the ability of CPFEM to qualitatively reproduce the experimental findings. Zeng *et al.* [33] developed a smoothed crystal plasticity finite element framework for modelling two-dimensional single crystals and polycrystals. Kim and Yoon [34] simulated the necking behaviour of AA 6022-T4 sheet using a CPFEM formulation involving four different continuum damage mechanics models, discussing the performance of such damage models when compared to experimental tests. Moreover, more advanced crystal plasticity phenomenological models, able to capture different deformation mechanisms besides slip, such as twinning in HCP crystals or non-Schmid effects in BCC crystals, are still under investigation. As a few recent examples, Abdolvand *et al.* [35] implemented in a finite element formulation a crystal plasticity model comprising twinning as well as slip in HCP materials, in order to simulate the deformation of a rolled Zircaloy-2 element. Wang *et al.* [36] proposed a physically-based crystal plasticity model including also de-twinning for HCP crystals and used it in a self-consistent model to simulate cyclic loading in a magnesium alloy. Lim *et al.*[37] developed a BCC crystal plasticity finite element model and employed it to simulate the deformation of tantalum oligo-crystals [38]. The authors compared numerical and experimental results

5

finding good agreement in terms of both in-plane and out-of-plane strain fields and lattice rotations. An interesting point raised by the authors was the lower agreement between predicted and measured fields at the grain boundaries, which prompted the authors to recommend more detailed grain boundary models in future studies.

The short review given above confirms the maturity of the CPFEM for the investigation of plasticity in crystalline solids and also the current engineering interest toward the development of new or more enriched models. On the other hand, while several boundary element formulations for elasto-plastic isotropic problems are present in the literature, see e.g. Refs.[39, 40, 41, 42, 43, 44, 45, 46], the authors are not aware of any boundary element application to anisotropic or crystal plasticity. A boundary element approach may in fact result in accurate stress/strain predictions at reduced discretization effort.

In the present work, a novel three-dimensional grain–boundary formulation for small strains crystal plasticity is presented for the first time. The boundary integral equations for anisotropic elasto-plasticity are given, Section 2. The presence of plastic flow is taken into account through an *initial strains* approach, which is commonly adopted in boundary element formulations for addressing elasto-plastic problems [39, 41]. The anisotropic kernels involved in the formulation are explicitly given, Section 2.2, and the strategy for numerical integration of the strongly singular volume integrals is discussed, Section 2.4. The adopted phenomenological continuum-based crystal plasticity description is discussed, Section 3, and the incremental/iterative grain-boundary algorithm for crystal plasticity is presented in a rate-dependent framework, Section 4. A grain–boundary *polycrystalline* implementation for crystal plasticity, based on previous works from Benedetti *et al.* [47, 48, 49, 50], is given, Section 5. The salient feature of the formulation is the expression of the problem in terms of intergranular variables only, namely grain–boundary displacements and tractions, also in presence of an interior plastic flow, which allows a remarkable reduction in the order of the numerical system, especially for polycrystalline analysis. Numerical tests are performed both for single crystals and crystal aggregates,

6

and they confirm the potential of the technique, Section 6. Directions of further investigation are discussed in Section 7, before the *Conclusions*.

2. Anisotropic elasto-plastic boundary element formulation

In the present section, the different ingredients of the boundary integral formulation of the crystal plasticity problem are presented. To maintain a unified notation, the basic equations are presented in rate form. This is a common procedure for time-dependent problems, such as creep or visco-plasticity. Rate-independent crystal plasticity problems, on the other hand, could be formulated in purely incremental terms, due to the to the lack of time-dependent effects. However, also rate-independent problems can be generally associated to a time-like parameter that plays the role of an ordering parameter, such as the load factor λ. Keeping this in mind, it is possible to retain a unique rate notation for both classes of problems.

Considered a generic domain $\mathcal{D} \subset \mathbb{R}^3$, representing a single crystal with specific symmetry undergoing elasto-plastic deformations, the proposed formulation is based on the use of a set of *boundary integral equations* representing the displacements and stresses of the points of the domain in terms of *boundary* integrals of the displacements and tractions of points on the *surface S* of the domain itself. When a region within $\mathcal{D}$ undergoes plastic slip, such equations are modified by the presence of some *volume* integral terms. The salient feature of the method is that only the boundary points carry degrees of freedom, irrespective of the presence of internal plastic regions, allowing a considerable reduction in the size of the solving system, which may be appealing in computational terms.

In the following sections, the previous outline is further developed and attention is devoted to the fundamental boundary integral equations, to the expressions of the integral kernels appearing in the equations and their numerical integration and to the form of the discrete algebraic systems.

7

2.1. Boundary integral equations

Let us consider the generic domain $\mathcal{D} \subset \mathbb{R}^3$, whose volume V is bounded by the external surface $S = \partial V$. When plastic deformations are considered within the context of the *small strains theory*, the *total* strain rates $\dot{\varepsilon}_{ij}$ can be expressed as the sum of *elastic* and *plastic* contributions

$$\dot{\varepsilon}_{ij} = \frac{1}{2} \left(\dot{u}_{i,j} + \dot{u}_{j,i} \right) = \dot{\varepsilon}_{ij}^e + \dot{\varepsilon}_{ij}^p. \tag{1}$$

where u_i denote the displacements components. The presence of plastic strains can be addressed in boundary element formulations by adopting an *initial strain* or *initial stress* approach [39, 40]: in the present work, the initial strain formulation is used, as it appears particularly suitable to the form of the crystal plasticity constitutive equations, see Section 3.

When some initial *plastic strains* $\dot{\varepsilon}_{jk}^p$ are present in $V_p \subset V$, the *displacement boundary integral equations* can be written, in rate form, as

$$c_{ij}(\mathbf{x})\dot{u}_j(\mathbf{x}) + \fint_S T_{ij}(\mathbf{x}, \mathbf{y})\, \dot{u}_j(\mathbf{y}) dS(\mathbf{y}) = \int_S U_{ij}(\mathbf{x}, \mathbf{y})\, \dot{t}_j(\mathbf{y}) dS(\mathbf{y}) +$$
$$+ \int_{V_p} \Sigma_{ijk}(\mathbf{x}, \mathbf{Y})\, \dot{\varepsilon}_{jk}^p(\mathbf{Y}) dV(\mathbf{Y}) \tag{2}$$

where $\mathbf{x}, \mathbf{y} \in S$ denote the *collocation* and *integration boundary* points respectively, $\mathbf{Y} \in V$ is a *volume* integration point, $\dot{u}_j$ and $\dot{t}_j$ are components of the boundary displacements and tractions, U_{ij}, T_{ij} and Σ_{ijk} are components of the displacement, traction and stress fundamental solutions respectively, see Section 2.2, $\fint$ denotes the Cauchy principal value integral due to the presence of the strongly singular kernels T_{ij} and c_{ij} are free terms stemming from the integration procedure over the domain boundary S, which are $c_{ij} = \delta_{ij}/2$ for regular boundary points; the volume integral is performed over the interior region $V_p \subset V$ undergoing plastic deformation, i.e. where $\dot{\varepsilon}_{jk}^p \neq 0$.

The boundary integral representation for the *strains* $\dot{\varepsilon}_{ij}$ at the generic interior point $\mathbf{X} \in V$ can be obtained applying the strain-displacement differential operator to the displacements boundary integral equations collocated at the interior

8

point $\mathbf{X} \in V$. In rate form, it is written as

$$\dot{\varepsilon}_{ij}(\mathbf{X}) + \int_S T_{ijk}^{\varepsilon}(\mathbf{X},\mathbf{y})\dot{u}_k(\mathbf{y})dS(\mathbf{y}) = \int_S U_{ijk}^{\varepsilon}(\mathbf{X},\mathbf{y})\dot{t}_k(\mathbf{y})dS(\mathbf{y}) +$$
$$+ \fint_{V_p} \Sigma_{ijkl}^{\varepsilon}(\mathbf{X},\mathbf{Y})\dot{\varepsilon}_{kl}^p(\mathbf{Y})dV(\mathbf{Y}) + f_{ijkl}^{\varepsilon}\dot{\varepsilon}_{kl}^p(\mathbf{X}),$$
(3)

where U_{ijk}^{ε}, T_{ijk}^{ε} and $\Sigma_{ijkl}^{\varepsilon}$ are obtained through suitable derivation from the kernels appearing in Eqs.(2), $f_{ijkl}^{\varepsilon}\dot{\varepsilon}_{kl}^p$ are the so called *free terms* [39, 40] and the Cauchy principal value integral $\fint$ is due to the presence of the strongly singular kernels $\Sigma_{ijkl}^{\varepsilon}$ in the volume integral. The expressions of both the kernels and free terms are given in Section 2.2, while the numerical treatment of the singular integrals is addressed in Section 2.4.

The boundary integral representation for the *stresses* $\dot{\sigma}_{ij}$ at the generic interior point $\mathbf{X} \in V$ is obtained from Eq.(3) using the constitutive relationships $\dot{\sigma}_{ij} = C_{ijkl}(\dot{\varepsilon}_{kl} - \dot{\varepsilon}_{kl}^p)$. In rate form, the stress boundary integral representation reads

$$\dot{\sigma}_{ij}(\mathbf{X}) + \int_S T_{ijk}^{\sigma}(\mathbf{X},\mathbf{y})\dot{u}_k(\mathbf{y})dS(\mathbf{y}) = \int_S U_{ijk}^{\sigma}(\mathbf{X},\mathbf{y})\dot{t}_k(\mathbf{y})dS(\mathbf{y}) +$$
$$+ \fint_{V_p} \Sigma_{ijkl}^{\sigma}(\mathbf{X},\mathbf{Y})\dot{\varepsilon}_{kl}^p(\mathbf{Y})dV(\mathbf{Y}) + f_{ijkl}^{\sigma}\dot{\varepsilon}_{kl}^p(\mathbf{X}),$$
(4)

where U_{ijk}^{σ}, T_{ijk}^{σ} and Σ_{ijkl}^{σ} and f_{ijkl}^{σ} can be obtained from the kernels and free terms appearing in Eqs.(3), suitably using the constitutive relationships.

185

2.2. Anisotropic kernels and free terms

The kernels U_{ij}, T_{ij}, Σ_{ijk}, U_{ijk}^{ε}, T_{ijk}^{ε}, $\Sigma_{ijkl}^{\varepsilon}$, U_{ijk}^{σ}, T_{ijk}^{σ}, Σ_{ijkl}^{σ} appearing in Eqs.(2-4) can be expressed in terms of the Green's functions for general anisotropic domains [51, 52, 53, 54, 55], which are reported in Appendix A for
190   the sake of completness.

Once the Green's functions G_{ij} and their derivatives have been introduced, the kernels appearing in Eq.(2) can be written

$$U_{ij} = G_{ij}, \qquad \Sigma_{ijk} = C_{jkpq}\frac{\partial G_{ip}}{\partial y_q}, \qquad T_{ij} = \Sigma_{ijk}\, n_k, \qquad (5)$$

where n_k are the components of the outward unit normal vector at the generic surface point at which the tractions are being computed. In Eq.(5), the right minor symmetry $C_{ijkl} = C_{ijlk}$, in conjunction with the summation rule with respect to repeated subscripts, has been used to simplify the expression of Σ_{ijk}. The kernels appearing in Eq.(3) are

$$U_{ijk}^\varepsilon = \frac{1}{2} \left(\frac{\partial G_{ik}}{\partial x_j} + \frac{\partial G_{jk}}{\partial x_i} \right), \quad \Sigma_{ijkl}^\varepsilon = \frac{C_{klpq}}{2} \frac{\partial}{\partial y_q} \left(\frac{\partial G_{ip}}{\partial x_j} + \frac{\partial G_{jp}}{\partial x_i} \right), \quad T_{ijk}^\varepsilon = \Sigma_{ijkl}^\varepsilon n_l, \tag{6}$$

which can be readily evaluated considering that $\partial G_{ij}/\partial x_k = -\partial G_{ij}\partial y_k$, due to the fact that G_{ij} depend on the difference between the positions of the collocation point $\mathbf{y}$ and the position of the integration point $\mathbf{x}$, i.e. $G_{ij} = G_{ij}(\mathbf{x} - \mathbf{y})$, see Appendix A.

The kernels appearing in Eq.(4) can be obtained considering that $U_{ijk}^\sigma = C_{ijpq} U_{pqk}^\varepsilon$ and $\Sigma_{ijkl}^\sigma = C_{ijrs} \Sigma_{rskl}^\varepsilon$, from which it follows

$$U_{ijk}^\sigma = C_{ijpq} \frac{\partial G_{pk}}{\partial x_q}, \qquad \Sigma_{ijkl}^\sigma = C_{ijrs} C_{klpq} \frac{\partial^2 G_{rp}}{\partial y_q \partial x_s}, \qquad T_{ijk}^\sigma = \Sigma_{ijkl}^\sigma n_l, \tag{7}$$

where again the right minor symmetry of the elasticity tensor and the summation rule have been used.

The coefficient f_{ijkl}^ε appearing in the free terms in Eq.(3) are given by

$$f_{ijkl}^\varepsilon = -\frac{1}{2} \int_{\Gamma(\mathbf{X})} \left(\Sigma_{ikl} n_j + \Sigma_{jkl} n_i \right) d\Gamma, \tag{8}$$

where $\Gamma(\mathbf{X})$ is the unit sphere centred in $\mathbf{X} \in V_p$ (note that the free terms are given by the products $f_{ijkl}^\varepsilon \dot{\varepsilon}_{kl}^p$). The coefficients f_{ijkl}^σ appearing in the free terms in Eq.(4) can be obtained considering that $\dot{\sigma}_{ij} = C_{ijkl} \left(\dot{\varepsilon}_{kl} - \dot{\varepsilon}_{kl}^p \right)$ and taking again into account the right minor symmetry and the subscripts summation rule, which lead to

$$f_{ijkl}^\sigma = -C_{ijpq} \left(\int_{\Gamma(\mathbf{X})} \Sigma_{pkl} n_q d\Gamma + \delta_{pk} \delta_{ql} \right). \tag{9}$$

It is worth noting that the Green's functions and all their derivatives, Appendix A, and then all the kernels K appearing in the formulation, can be written as a

10

product between a singular function, depending on the distance r between the collocation ($\mathbf{x}$ or $\mathbf{X}$) and integration ($\mathbf{y}$ or $\mathbf{Y}$) points and a finite part $\Psi(\theta, \phi)$, known as *modulation function*, depending on the collocation-integration direction and the material properties:

$$K = \frac{1}{r^\beta} \cdot \Psi(\theta, \phi) \tag{10}$$

where β is specific to the considered kernel. The previous form is useful in the evaluation of the singular integrals appearing in the boundary integral representation.

2.3. Numerical discretisation

In the initial strains approach [39, 41], the crystal plasticity problem is closed considering the displacement and stress boundary integral equations, Eq.(2) and Eq.(4), together with the crystal plasticity constitutive equations given in Section 3. In order to write the discrete counterpart of the boundary integral equations, the following steps are followed:

- The boundary S and the volume V of the analysed domain are subdivided into sets of non-overlapping surface and volume elements: in the present work, the surface has been discretised using the strategy developed in [50], where a specific grain–boundary meshing algorithm suitably combining continuous and semi–discontinuous triangular and quadrangular two-dimensional elements has been implemented in order to tackle and reduce the high computational costs of the polycrystalline problem; on the other hand, sub-parametric elements[1] have been used for the volume (constant strains within each linear internal volume cell);

- The unknown fields, namely displacements and tractions on the surface

---

[1]In *sub-parametric* elements the order of interpolation of the unknown fields is lower than the order of interpolation of the geometry.

11

and plastic strains in the volume, are expressed in terms of nodal values

²⁴⁰ and suitable shape functions;

- Eq.(2) is written for every boundary discretisation node and it is then numerically integrated;

- Eq.(4) is written for every internal point and it is then numerically integrated.

²⁴⁵ Grouping the discrete displacement equations written for each boundary node leads to the system

$$\mathbf{H}\,\dot{\mathbf{u}} = \mathbf{G}\,\dot{\mathbf{t}} + \mathbf{D}\dot{\varepsilon^p},\tag{11}$$

where $\dot{\mathbf{u}}$ and $\dot{\mathbf{t}}$ contain the components of the nodal values of the boundary displacements and tractions, which are the *primary unknowns* of the problem, the matrices $\mathbf{H}$ and $\mathbf{G}$ stem from the integration of the kernels U_{ij} and T_{ij}, over the boundary of the considered domain, $\dot{\varepsilon^p}$ contain the components of the nodal values of plastic strains and the matrix $\mathbf{D}$ is generated from the numerical integration of Σ_{ijk} over the interior volume region undergoing plastic flow.

To solve the crystal plasticity problem, Eq.(11) has to be used with the discretised version of the stress integral equation (4) that, written for a specific internal point, reads

$$\dot{\boldsymbol{\sigma}}\left(\mathbf{X}\right) = \mathbf{G}_X^\sigma\,\dot{\mathbf{t}} - \mathbf{H}_X^\sigma\,\dot{\mathbf{u}} + \mathbf{D}_X^\sigma\,\dot{\varepsilon^p}\tag{12}$$

where $\dot{\boldsymbol{\sigma}}\left(\mathbf{X}\right)$ contains the components of stress at the generic interior point $\mathbf{X}$, the matrices $\mathbf{H}_X^\sigma$ and $\mathbf{G}_X^\sigma$ stem from the numerical integration of the kernels $U_{ijk}^\sigma\left(\mathbf{X},\mathbf{y}\right)$ and $T_{ijk}^\sigma\left(\mathbf{X},\mathbf{y}\right)$ over the domain's boundary, and $\mathbf{D}_X^\sigma$ stems from
²⁵⁰ the integration of the kernels $\Sigma_{ijlk}^\sigma\left(\mathbf{X},\mathbf{Y}\right)$ over the interior region undergoing plastic flow, including the corresponding free terms.

Eqs.(11-12) must be used in conjunction with the suitable boundary conditions and the constitutive crystal plasticity equations for the solution of the grain-boundary elasto-plastic problem, as will be described in Section 4. The
²⁵⁵ interested reader is referred to references [39, 40, 41] for further details about

12

the boundary element method.

2.4. Numerical integration and singular integrals

To obtain the discrete equations introduced above, it is necessary to accu-
rately evaluate the *singular* integrals appearing in Eqs. (2) and (4). While the
singular integrals appearing in the displacement equations, Eq.(2), have been
widely considered in the literature, the authors are not aware of any previous
work considering the integration of the singular kernels Σ_{ijkl} *for the anisotropic*
case. In this section, the procedures used for the evaluation of the singular
integrals are briefly recalled, and the strategy used for treating the integrals
involving Σ_{ijkl} is described.

Considering Eq.(2), the weak singularity induced on the boundary by U_{ij} is
treated subdividing the singular elements into triangles and representing each
sub-triangle as a quadrangle collapsed into the singular point; the strong singu-
larity induced by T_{ij}, treated as a Cauchy singular value, is tackled using rigid
body considerations [40, 41]; the volume terms appearing in Eq.(2) may give
rise to weak singularities only when the plastic region reaches the boundary: in
this case, the interested volume cells are subdivided into sub-tetrahedra, which
afterwards are represented as 8-node cubes collapsed into the singular point.

In the strain and stress integral equations, Eqs.(3-4), since constant volume
cells are used in the implementation, the collocation points $\mathbf{X}$ always fall in the
interior domain, being the centroids of the volume cells. For such a reason,
the boundary integrals may become at most nearly singular, and this happens
when the plastic region reaches the boundary. Nearly singular integrals are
simply evaluated through boundary element subdivision. The *volume* integrals,
on the contrary, must be treated in the Cauchy singular value sense, being the
kernels Σ_{ijkl} strongly singular in the volume.

In the present work, the starting point for the evaluation of the volume Cauchy
singular values is the work by Gao and Davies [56], who, for isotropic materials,
have shown that the integral of Σ_{ijkl} over the singular volume cell V_s can be

13

expressed as

$$\oint_{V_s} \Sigma_{ijkl}\, dV = \oint_{V_s} \frac{1}{r^3} \Psi_{ijkl}\, dV = \int_{S_s} \Sigma_{ijkl}\, r_p n_p \ln(r)\, dS, \qquad (13)$$

as long as the condition

$$\int_{\Gamma(\mathbf{X})} \Psi_{ijkl}\, d\Gamma = 0, \qquad (14)$$

involving the integral of the modulation function Ψ_{ijkl} over the unit sphere $\Gamma(\mathbf{X})$ centred in the singular point $\mathbf{X}$, is satisfied. In Eq.(13), $S_s = \partial V_s$ is the external boundary of the singular volume sub-cell V_s. Gao and Davies [56] demonstrated Eq.(14) for isotropic materials, taking into account the explicit analytical form of the isotropic fundamental solutions. In the anisotropic case, the analytical expression of Ψ_{ijkl} is not available, being the Green's functions expressed in a closed integral form. However, in the present work, the condition expressed by Eq.(14) has been numerically tested for the considered anisotropic materials, providing the sufficient condition for the application of Eq.(13), which holds also in the anisotropic case.

3. Crystal plasticity phenomenological modelling

Crystal plasticity can be generally modeled through *phenomenological* or *physically-based* approaches [2]. Moreover, the crystallographic slip within single crystals can be idealized as either *rate-dependent* or *rate-independent*. In the present work, a phenomenological rate-dependent description is adopted. In the present section, an introductory functional description of crystal slip is briefly recalled for the sake completeness.

The slip over a specific slip plane α identified by the unit normal vector $\mathbf{n}^\alpha$, and along a specific direction identified by the unit vector $\mathbf{s}^\alpha$, is *activated* by the *Schmid resolved shear stress*

$$\tau^\alpha = s_i^\alpha \sigma_{ij} n_j^\alpha, \qquad (15)$$

14

which triggers the corresponding *slip* or *shear rate*

$$\dot{\gamma}^\alpha = \Psi^\alpha \left(\frac{\tau^\alpha}{\tau_c^\alpha} \right) \tag{16}$$

where Ψ^α expresses a specific *flow rule* and $\tau_c^\alpha = \Phi(\boldsymbol{\gamma}, \dot{\boldsymbol{\gamma}})$, is a certain *critical shear stress*, which plays the role of a *state variable* for the slip system α. τ_c^α generally depends on the *accumulated slips* $\gamma^\beta = \int_t |\dot{\gamma}^\beta| dt$ and on the slip rates $\dot{\gamma}^\beta$ on *all* the N_s slip systems, that have been collected into the vectors $\boldsymbol{\gamma} = \left(\gamma^1, \cdots, \gamma^{N_s} \right)$ and $\dot{\boldsymbol{\gamma}} = \left(\dot{\gamma}^1, \cdots, \dot{\gamma}^{N_s} \right)$ to indicate the functional dependence of τ_c^α. To avoid possible confusion, the sum of the accumulated slips γ^α over all the N_s slip systems, which is defined as $\gamma \equiv \sum_\alpha \gamma^\alpha$, will be referred to as the *overall cumulative slip*.

As plastic slip accumulates, τ_c^α evolves as

$$\dot{\tau}_c^\alpha = \Xi^\alpha(\boldsymbol{\gamma}, \dot{\boldsymbol{\gamma}}) \tag{17}$$

where Ξ^α expresses some specific *hardening law*. Eqs.(15–17) hold $\forall \alpha = 1, \cdots, N_s$. Once the slip rates (or slip increments, in rate-independent formulations) are known, the plastic strains rate (or increment) at a point in the crystal can be expressed as

$$\dot{\varepsilon}_{ij}^p = \frac{1}{2} \sum_{\alpha=1}^{N_s} \dot{\gamma}^\alpha \left(n_i^\alpha \, s_j^\alpha + s_i^\alpha \, n_j^\alpha \right). \tag{18}$$

The developed formulation can be coupled with different types of flow and hardening rules. For completeness, the flow and hardening rules used in this work are reported in Appendix B.

4. The grain-boundary incremental-iterative algorithm for crystal plasticity

Following Refs.[57, 39], in the framework of the initial strain formulation the elasto-plastic grain-boundary problem can be expressed in terms of *accumulated* values of displacements $\mathbf{u}$, tractions $\mathbf{t}$ and plastic strains $\boldsymbol{\varepsilon}^p$. Eq.(2) can then be

15

rewritten as

$$\mathbf{H}\,\mathbf{u} = \mathbf{G}\,\mathbf{t} + \mathbf{D}\,\boldsymbol{\varepsilon}^p \qquad \xrightarrow{\;BCs\;} \qquad \mathbf{A}\,\mathbf{q} = \boldsymbol{\phi}(\lambda) + \mathbf{D}\,\boldsymbol{\varepsilon}^p \qquad\qquad \text{(19a,b)}$$

where the reordering induced by the enforcement of the boundary conditions (BCs) is indicated. In Eq.(19b), the matrix $\mathbf{A}$ contains a selection of columns from $\mathbf{H}$ and $\mathbf{G}$ corresponding to *unknown* components of boundary displacements and tractions, collected in the unknowns vector $\mathbf{q}$; the vector $\boldsymbol{\phi}(\lambda)$ is a linear combinations of the columns from $\mathbf{H}$ and $\mathbf{G}$ corresponding to *known* components of boundary displacements and tractions, weighted by the known values of displacements and tractions themselves, which in general depend on a load factor λ that plays the role of an ordering parameter; the matrix $\mathbf{D}$ stems from the volume integration over the interior region undergoing plastic flow and $\boldsymbol{\varepsilon}^p$ contains the components of the plastic strains within the volume discretization cells, to be determined through an iterative algorithm.

On the other hand, Eq.(12) can be rewritten, in terms of accumulated values, as

$$\boldsymbol{\sigma} = \mathbf{G}^\sigma \mathbf{t}(\lambda) - \mathbf{H}^\sigma \mathbf{u}(\lambda) + \mathbf{D}^\sigma \boldsymbol{\varepsilon}^p \qquad\qquad \text{(20)}$$

where the dependence on the interior point $\mathbf{X}$ is omitted for readability and no distinction is made between known and unknown values of boundary displacements and tractions, due to the fact that the previous equation is generally used in a *post-processing* stage, after Eq.(19b) has been solved.

The incremental iterative algorithm used to solve the crystal plasticity problem is described in Algorithm 1, which is commented in the following. In the Algorithm, the superscript α refers to the slip systems while the subscript $k = 0, 1, ..., N_{conv}$ indicates the current iteration. On the other hand, e refers to the interior volume cells, but it is not used as sub/superscript, to avoid making the notation too heavy. Once the solution corresponding to the load factor λ has been found, the load increment $\Delta\lambda = \dot{\lambda}\Delta t$, where $\dot{\lambda}$ is the *loading rate*, is introduced and the iterative cycle starts initialising the accumulated slip increments ($\Delta\gamma^\alpha$), the overall cumulative slip increments ($\Delta\gamma$), the critical stress increments ($\Delta\tau_c^\alpha$) and the plastic strain increments ($\Delta\boldsymbol{\varepsilon}^p$) (*steps* 3-6).

16

In *step* 8, Eq.(19b) is solved for the current iteration after suitably updating the right-hand side (note that, in the Algorithm, $\boldsymbol{\varepsilon}^p(\lambda)$ collects the *converged* plastic strain components up to the load level λ, but not including the effects of the last increment $\Delta\lambda$).

The updated computed values of boundary displacements and tractions are then used in *step* 9 to compute the internal stress $\boldsymbol{\sigma}_{(k)}$ at each volume cell's centroid, using Eq.(20). The internal stresses are in turn used, in *step* 10, to obtain the resolved shear stresses $\tau_{(k)}^\alpha$ on each slip plane through Eq.(15) and then the corresponding increments $\Delta\tau_{(k)}^\alpha$ with respect to the last converged values $\tau^\alpha(\lambda)$.

In *step* 11, the values $\Delta\tau_{(k)}^\alpha$ are used to compute the slip and critical stress increments using the reported expressions, where $\theta \in [0,1]$ is an interpolation parameter for which a value between 0.5 and 1 is suggested [58], $\dot{\gamma}^\alpha(\lambda)$ and $\dot{\tau}_c^\alpha(\lambda)$ are the converged values of slip rate and critical shear stress at λ and

$$\dot{\gamma}_{(k)}^\alpha(\lambda + \Delta\lambda) = \dot{\gamma}^\alpha(\lambda) + \left.\frac{\partial\dot{\gamma}^\alpha}{\partial\tau^\alpha}\right|_\lambda \Delta\tau_{(k)}^\alpha + \left.\frac{\partial\dot{\gamma}^\alpha}{\partial\tau_c^\alpha}\right|_\lambda \Delta\tau_{c(k)}^\alpha \tag{21}$$

$$\dot{\tau}_{c(k)}^\alpha(\lambda + \Delta\lambda) = \Xi^\alpha\left[\boldsymbol{\gamma}(\lambda) + |\Delta\boldsymbol{\gamma}_{(k)}|, \dot{\boldsymbol{\gamma}}(\lambda + \Delta\lambda)\right] \tag{22}$$

where the vector $\Delta\boldsymbol{\gamma}_{(k)} = \left(\Delta\gamma_{(k)}^1, \cdots, \Delta\gamma_{(k)}^{N_s}\right)$ collects the increments of accumulated slips over the N_s slip systems.

At this point the overall cumulative slip increment $\Delta\gamma_{(k+1)}$ is computed for each volume cell and the convergence condition is checked. If the convergence is met then the accumulated slips, the resolved shear stresses and the critical shear stresses are updated and stored and another load increment can be introduced and computed if needed. If the convergence is not met, the plastic strain increments are computed using Eq.(18), the iteration counter k is updated and another iteration is started (*steps* 12-21).

5. Grain–boundary polycrystalline implementation

The grain–boundary crystal plasticity formulation proposed above has also been developed and implemented for polycrystalline microstructures, in the

17

Algorithm 1 CPBEM algorithm

START

1: Set $\quad \lambda := 0$

2: **while** $(\lambda < \lambda_f)$ **do**

3: $\qquad$ Set $\quad \Delta\lambda := \dot{\lambda}\Delta t, \qquad k := 0$

4: $\qquad \forall e \quad$ set $\quad \Delta\boldsymbol{\varepsilon}^p_{(k=0)} := \mathbf{0}, \qquad \Delta\gamma_{(k=0)} := 0$

5: $\qquad \forall e, \alpha, \quad$ set $\quad \Delta\gamma^\alpha_{(k=0)} := 0, \qquad \Delta\tau^\alpha_{c\,(k=0)} := 0$

6: $\qquad$ Set $\quad$ CONVERGED $:=$ .FALSE.

7: $\qquad$ **while** (.NOT.CONVERGED) **do**

8: $\qquad\qquad$ Solve $\mathbf{A}\,\mathbf{q}_{(k)} = \boldsymbol{\phi}(\lambda + \Delta\lambda) + \mathbf{D} \cdot \left[\boldsymbol{\varepsilon}^p(\lambda) + \Delta\boldsymbol{\varepsilon}^p_{(k)}\right];$ $\qquad \triangleright$ Eq.(19a,b)

9: $\qquad\qquad \forall e$ solve

$$\boldsymbol{\sigma}_{(k)} = \mathbf{G}^\sigma\,\mathbf{t}_{(k)} - \mathbf{H}^\sigma\,\mathbf{u}_{(k)} + \mathbf{D}^\sigma \cdot \left[\boldsymbol{\varepsilon}^p(\lambda) + \Delta\boldsymbol{\varepsilon}^p_{(k)}\right]; \qquad \triangleright \text{Eq.(20)}$$

10: $\qquad\qquad \forall e, \alpha$ compute $\tau^\alpha_{(k)}$ and $\Delta\tau^\alpha_{(k)} := \tau^\alpha_{(k)} - \tau^\alpha(\lambda)$ $\qquad \triangleright$ Eq.(15)

11: $\qquad\qquad \forall e, \alpha$ compute $\begin{cases} \Delta\gamma^\alpha_{(k+1)} := \left[(1-\theta)\,\dot{\gamma}^\alpha(\lambda) + \theta\,\dot{\gamma}^\alpha_{(k)}(\lambda + \Delta\lambda)\right]\Delta t \\[2mm] \Delta\tau^\alpha_{c\,(k+1)} := \left[(1-\theta)\,\dot{\tau}^\alpha_c(\lambda) + \theta\,\dot{\tau}^\alpha_{c(k)}(\lambda + \Delta\lambda)\right]\Delta t \end{cases}$

$\qquad\qquad\qquad\qquad\qquad\qquad\qquad\qquad\qquad\qquad\qquad\qquad\qquad \triangleright$ Eqs.(21-22)

12: $\qquad\qquad \forall e$ compute $\Delta\gamma_{(k+1)} := \sum_{\alpha=1}^{N_s} \left|\Delta\gamma^\alpha_{(k+1)}\right|;$

13: $\qquad\qquad$ **if** $\left(\forall e \quad \left|\Delta\gamma_{(k+1)} - \Delta\gamma_{(k)}\right| < \epsilon_{conv}\right)$ **then**

14: $\qquad\qquad\qquad$ Set CONVERGED $:=$ .TRUE.

15: $\qquad\qquad$ **else**

16: $\qquad\qquad\qquad \forall e$ compute $\Delta\boldsymbol{\varepsilon}^p_{(k+1)};$ $\qquad\qquad\qquad\qquad \triangleright$ Eq.(18)

17: $\qquad\qquad\qquad$ Set $\quad k := k + 1$

18: $\qquad\qquad$ **end if**

19: $\qquad$ **end while**

20: $\qquad \forall e, \alpha$ update and store $\begin{cases} \gamma^\alpha(\lambda + \Delta\lambda) := \gamma^\alpha(\lambda) + \left|\Delta\gamma^\alpha_{(k+1)}\right| \\[2mm] \tau^\alpha(\lambda + \Delta\lambda) := \tau^\alpha(\lambda) + \Delta\tau^\alpha_{(k+1)} \\[2mm] \tau^\alpha_c(\lambda + \Delta\lambda) := \tau^\alpha_c(\lambda) + \Delta\tau^\alpha_{c\,(k+1)} \end{cases}$

21: $\qquad$ Set $\lambda := \lambda + \Delta\lambda;$

22: **end while**

$\quad$ **EXIT**
---

framework developed by Sfantos and Alibadi (2D) [59, 60] and by Benedetti

et al. (3D) [47, 48, 49, 50]. In the present Section, such polycrystalline imple-
mentation is described.

5.1. Boundary integral equations

In a polycrystalline framework, each grain can be thought as an anistropic
elasto-plastic domain with a specific orientation in the three-dimensional space.
In the present work, the polycrystalline morphology is represented as a Voronoi-
Laguerre tessellation contained within a bounding domain $\mathcal{V}$: each grain is
then a convex polyhedron bounded by convex polygonal flat faces, see Fig.(1).
Following Ref.[47], Eqs.(2) can be rewritten, for a generic point $\mathbf{x}_g$ belonging to
the surface S_g of a generic grain g, as

$$\widetilde{c}_{ij}(\mathbf{x}_g)\dot{\widetilde{u}}_j(\mathbf{x}_g) + \fint_{S_g} \widetilde{T}_{ij}\left(\mathbf{x}_g, \mathbf{y}_g\right)\dot{\widetilde{u}}_j(\mathbf{y}_g)dS(\mathbf{y}_g) = \int_{S_g} \widetilde{U}_{ij}\left(\mathbf{x}_g, \mathbf{y}_g\right)\dot{\widetilde{t}}_j(\mathbf{y}_g)dS(\mathbf{y}_g) +$$
$$+ \int_{V_{pg}} \Sigma_{ijk}(\mathbf{x}_g, \mathbf{Y}_g)\dot{\varepsilon}_{jk}(\mathbf{Y}_g)dV(\mathbf{Y}_g)$$

(23)

where V_{pg} is the interior grain's volume undergoing plastic strain and the tilde
($\widetilde{}$) denote quantities expressed in *local* reference systems chosen on *each* grain
face, so to express *boundary* displacements and tractions in terms of components
normal and tangent to the grain faces themselves, to simplify the implementa-
tion of general inter-granular conditions [48]. It is worth noting that only the
integral terms containing boundary variables are expressed in local coordinates,
while generally the volume terms, where the plastic strains $\dot{\varepsilon}_{ij}$ components ap-
pear, can be expressed in any other convenient reference system, e.g. a global
or grain's material reference system.

Analogously, Eq.(4) can be rewritten, for a generic point $\mathbf{X}_g$ inside the generic

19

grain g

$$\dot{\sigma}_{ij}(\mathbf{X}_g) + \int_{S_g} \widetilde{T}^{\sigma}_{ijk}(\mathbf{X}_g, \mathbf{y}_g)\,\dot{\widetilde{u}}_k(\mathbf{y}_g)dS(\mathbf{y}_g) = \int_{S_g} \widetilde{U}^{\sigma}_{ijk}(\mathbf{X}_g, \mathbf{y}_g)\,\dot{\widetilde{t}}_k(\mathbf{y}_g)dS(\mathbf{y}_g) +$$

$$+ \fint_{V_{pg}} \Sigma^{\sigma}_{ijkl}(\mathbf{X}_g, \mathbf{Y}_g)\,\dot{\varepsilon}^p_{kl}(\mathbf{Y}_g)dV(\mathbf{Y}_g) + f^{\sigma}_{ijkl}\,\dot{\varepsilon}^p_{kl}(\mathbf{X}_g). \quad (24)$$
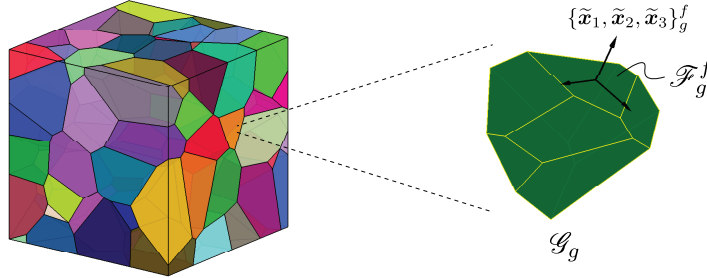
Figure 1: Polycrystalline morphology generated through Laguerre-Voronoi tessellations: each grain is a convex polyhedron bounded by convex polygonal faces. A *local* reference system is set on *each* face, so to express inter-granular variables in *varying* local coordinates.

5.2. Numerical discretization

Eqs.(23-24), suitably used for each grain, are the basis for the construction of the numerical polycrystalline model. As mentioned above, each grain is a convex polyhedron bounded by convex polygonal faces. In the present work, the boundary discretisation process is based on the subdivision of each grain's face into non-overlapping triangles/quadrangles, according to the strategy described in Ref.[50]. However, for crystal plasticity modeling, besides the grain-boundary meshes used in previous studies [47, 48, 49, 50], also volume meshes for the grains' interior must be used, to take into account the occurrence of plastic slip. In the present work, the volume meshes for polycrystalline Voronoi–type microstructures are generated using Hypermesh (`http://www.altairhyperworks.com`), which subdivides the volume into non-overlapping tetrahedra. In general, no

20

conformity between boundary meshes and interior volume meshes is required, which results in a relatively more complex implementation counterbalanced by simpler data preparation. The boundary polygons and the volume tetrahedra provide the geometrical support to express boundary displacements and tractions and volume strains and stresses fields through shape functions and nodal values of displacements, tractions, strains and stresses. Linear shape functions are used for the boundary fields [50], while the plastic strains are assumed constant within each volume tetrahedron.

Once the boundary and volume meshes have been generated for all the grains of the aggregate, Eq.(23) can be written for each boundary node of each grain, and numerically integrated. Following the procedures detailed in Refs.[47, 50], taking into account the presence of the volume terms and enforcing the *external* boundary conditions (i.e. displacement and tractions conditions on the grains' faces lying on the exterior surface of the bounding box $\mathcal{V}$), Eq.(19b) can be written for each grain g

$$\mathbf{A}_g\,\mathbf{q}_g = \boldsymbol{\phi}_g(\lambda) + \mathbf{D}_g\boldsymbol{\varepsilon}_g^p \qquad \forall g = 1, ..., N_g \tag{25}$$

where the symbols have the same meaning as in Eq.(19b), with the additional consideration that now $\mathbf{q}_g$ collects also the components of the unknown *inter-granular* displacements and tractions. The model for the polycrystalline aggregate is then obtained using Eq.(25) for each grain and enforcing the suitable inter-granular conditions, which leads to

$$
\begin{bmatrix}
\mathbf{A}_1 & \mathbf{0} & \cdots & \mathbf{0} \\
\mathbf{0} & \mathbf{A}_2 & \cdots & \mathbf{0} \\
\vdots & \vdots & \ddots & \vdots \\
\mathbf{0} & \mathbf{0} & \cdots & \mathbf{A}_{N_g} \\
\longleftarrow & \mathbf{I} & \longrightarrow
\end{bmatrix}
\begin{bmatrix}
\mathbf{q}_1 \\
\mathbf{q}_2 \\
\vdots \\
\mathbf{q}_{N_g}
\end{bmatrix}
=
\begin{bmatrix}
\boldsymbol{\phi}_1 \\
\boldsymbol{\phi}_2 \\
\vdots \\
\boldsymbol{\phi}_{N_g} \\
\mathbf{0}
\end{bmatrix}_\lambda
+
\begin{bmatrix}
\mathbf{D}_1 & \mathbf{0} & \cdots & \mathbf{0} \\
\mathbf{0} & \mathbf{D}_2 & \cdots & \mathbf{0} \\
\vdots & \vdots & \ddots & \vdots \\
\mathbf{0} & \mathbf{0} & \cdots & \mathbf{D}_{N_g} \\
\mathbf{0} & \mathbf{0} & \cdots & \mathbf{0}
\end{bmatrix}
\begin{bmatrix}
\boldsymbol{\varepsilon}_1^p \\
\boldsymbol{\varepsilon}_2^p \\
\vdots \\
\boldsymbol{\varepsilon}_{N_g}^p
\end{bmatrix}
\tag{26}
$$

or more compactly

$$
\begin{bmatrix}
\mathbf{A} \\
\mathbf{I}
\end{bmatrix}
\mathbf{q} =
\begin{bmatrix}
\boldsymbol{\phi}(\lambda) \\
\mathbf{0}
\end{bmatrix}
+
\begin{bmatrix}
\mathbf{D} \\
\mathbf{0}
\end{bmatrix}
\boldsymbol{\varepsilon}^p,
\tag{27}
$$

21

where $\mathbf{I}$ is the matrix implementing the considered interface conditions: in the present work, only perfect bonding between contiguous grains is assumed, so that $\mathbf{I}$ contains just zeros and ± 1, to enforce the conditions $\mathbf{u}_a = \mathbf{u}_b$ and $\mathbf{t}_a = -\mathbf{t}_b$ for pairs of contiguous interface points belonging to the generic grains a and b. In the solution algorithm, system (27) is used in conjunction with the stress equation

$$\boldsymbol{\sigma} = \mathbf{G}_g^\sigma \, \mathbf{t}_g(\lambda) - \mathbf{H}_g^\sigma \, \mathbf{u}_g(\lambda) + \mathbf{D}_g^\sigma \boldsymbol{\varepsilon}^p \qquad \forall g = 1, ..., N_g, \tag{28}$$

which is used to evaluate the stress at each interior test point within each grain. It is worth noting that, being Eq.(28) used after the solution of Eq.(27), in a post-process stage within each iteration, it can be used for each grain separately, as $\mathbf{u}_g$ and $\mathbf{t}_g$ are known.

5.3. Polycrystalline iterative system solution

The analysis of crystal-plasticity in polycrystalline aggregates poses a remarkable computational task. The problem is tackled employing the incremental/iterative procedure described in Section 4, with Eq.(27) used to update the accumulated values of displacements and tractions for all the aggregate and Eq.(28) used to compute the stress components at each interior test point within each grain, which then trigger, through the resolved shear stresses, the plastic flow. In the present work, only the rate–dependent algorithm is tested for the polycrystalline case, as the rate–independent implementation, in the simple form presented in Section 4, gave difficult or no convergence. The implementation of more sophisticated rate–independent schemes [8] goes beyond the scope of the present work and is left for open to further investigation. Convergence is reached for the aggregate when condition at *step* 13 of Algorithm 1 is satisfied for *each* interior test point within *each* grain, which considerably increases the required computational effort.

From the purely numerical/computational point of view, System (27) is solved using a slight modification of the procedure in described in Refs.[48, 50], to

22

take into account the iterative update of the plastic strains ε^p. Being the system highly sparse, PARDISO (http://www.pardiso-project.org/) [61, 62, 63] is used as solver. In terms of computational effectiveness, further research could be addressed at the development of specialized high efficiency solvers, based for example on the use of the hierarchical format in conjunction with iterative solution strategies [64, 65].

6. Numerical tests

In this Section, the developed and implemented formulation is numerically and computationally assessed. The phenomenological framework by Bassani and Wu [12] is used in the first series of tests performed in the present work, considering FCC copper as benchmark material. The single crystal properties as well as the slip systems numbering used in the present study coincide with those in Refs.[66, 12]. The elastic constants for FCC copper single crystals are: $C_{11} = 170\,\text{GPa}$; $C_{12} = 124\,\text{GPa}$; $C_{44} = 64.5\,\text{GPa}$. The crystal plasticity parameters are summarised in Table 1.

Table 1: Crystal plasticity parameters for copper single crystals and strength amplitude factors $f_{\alpha\beta}$ for the FCC single-crystal slip systems from [12].

τ_0	τ_s	h_s	h_0	γ_p	$\dot{\gamma}_0$	n	q
$17\,\text{MPa}$	$1.3 \cdot \tau_0$	$1.5 \cdot \tau_0$	$90 \cdot \tau_0$	0.001	$0.001\,s^{-1}$	50	0
				No junction, $f_{\alpha\beta} = a_1 = 8.0$			
				Hirth lock, $f_{\alpha\beta} = a_2 = 8.0$			
	Cross hardening moduli			Coplanar interaction, $f_{\alpha\beta} = a_3 = 8.0$			
				Glissile junction, $f_{\alpha\beta} = a_4 = 15.0$			
				Sessile junction, $f_{\alpha\beta} = a_5 = 20.0$			

6.1. Single crystal tests

To assess the accuracy and numerical performance of the formulation, tests on a single crystal are performed first. The analysed domain is a cubical crystal, with the edges aligned with the reference system and subjected to uniaxial stress acting along the x_3 direction.

In Fig.(2) the behaviour of the implemented scheme is tested with respect to the value of the rate sensitivity n appearing in Eq.(B.1), for the three different crystallographic loading directions [001], [111] and [632], chosen as in [12] for comparative purposes. In all the tests, the loading rate $\dot{\lambda}$, is always set as $\dot{\lambda} = 10^{-3} s^{-1}$. The curves plot the stress component σ_{33} at the centroid of the cube versus the strain component ε_{33} at the same point. It is worth noting that nominal components of strains are considered, being the developed formulation valid for small strains. However, strains up to 10% are plotted, to investigate when the small strains assumption breaks down: it is interesting to note as, up to this value of strains, the converged curves match reasonably well with those reported in [12], which have been replicated in the figure using a simple rate-independent scheme and represented with dashed lines. It is confirmed that, as n rises, the rate-dependent scheme simulates a rate-independent process, although the convergence is not the same for all directions, being noticeably slower (with respect to n) for the direction [632]. Also, it is interesting to note that for the [001] and [111] loading directions, the rate-dependent scheme predicts a lower bound for the stress, whereas for the [632] loading direction it predicts an upper bound.

In the following series of tests, the single crystal response is tested against different domain volume meshes, in order to assess the robustness of the computational homogenization scheme that will be used in the polycrystalline tests. Unlike the curves reported in Figs.(2), which are obtained considering the values of stress and strain at the centroid of the cubic single crystal domain, the stress-strain curves in the subsequent part of this work are obtained as averaged results of the stress and the strain fields over the crystalline or polycrystalline
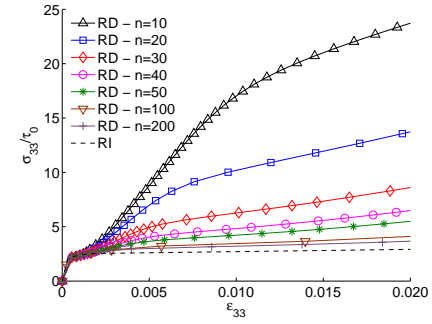
24
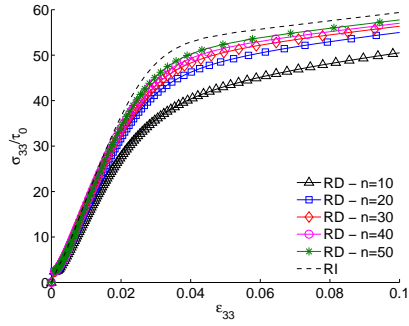
(a) Loading direction [001]
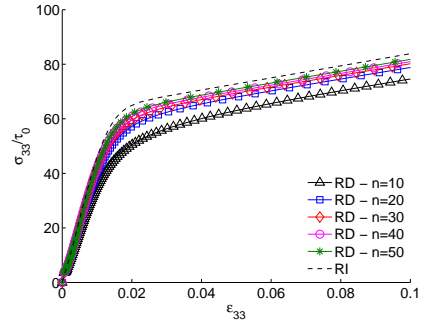
(b) Loading direction [111]
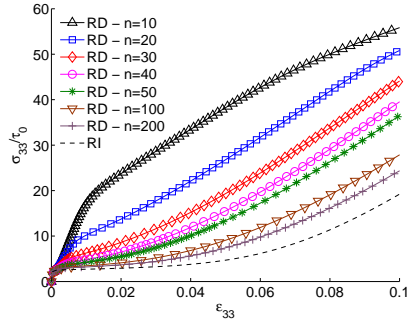
(c) Loading direction [632]

(d) Loading direction [632]

Figure 2: Effect of the rate sensitivity parameter n for three different loading crystallographic directions. Plot (d) shows a zoom from plot (c). It is apparent as the rate-dependent results converge to the rate-independent ones with increasing values of n.

domain. Strain and stress volume averages are given by

$$\Gamma_{ij} = \frac{1}{V}\int_V \gamma_{ij}(\mathbf{X})dV(\mathbf{X}) = \frac{1}{2V}\int_S [u_i(\mathbf{x})n_j(\mathbf{x}) + u_j(\mathbf{x})n_i(\mathbf{x})]dS(\mathbf{x}) \qquad (29)$$

$$\Sigma_{ij} = \frac{1}{V}\int_V \sigma_{ij}(\mathbf{X})dV(\mathbf{X}) = \frac{1}{V}\int_S x_i(\mathbf{x})t_j(\mathbf{x})dS(\mathbf{x}) \qquad (30)$$

where S and V represents the boundary and the volume of the domain, respectively. The terms involving the surface integrals allow to write the volume averages in terms of boundary displacements and tractions, which are the primary variables of the model. The terms involving the volume integrals, on the other hand, are be obtained as the weighed sum of the strains and stresses computed at the centroids of the tetrahedra, i.e. $\int_V(\cdot)dV = \sum_e(\cdot)_e V_e$ being V_e the volume of the e-th volume element. The comparison between the volume averages computed using the volume and the surface integrals can be used as a tool to assess the accuracy in the integration of the kernels in the displacement and stress boundary integral equations.

Fig.(3) shows four surface and volume meshes of a cubic domain. Following [47], the surface and volume meshes of the crystalline domain are built considering an as uniform as possible mesh size, which is computed as the average length of the edges of the considered crystals divided by a mesh density parameter d_m, see [47]. In the considered case, the average edge length is clearly the cube edge. Figs.(3a,e), Figs.(3b,f), Figs.(3c,g), Figs.(3e,h) correspond to $d_m = 2, 3, 4, 5$, respectively. Although they may not represent the best meshing choice for a cubic domain, the combination of triangular and quadrangular elements in the surface meshes and the tetrahedra in the volume meshes have been found particularly appropriate to adapt to the geometrical variability of general Voronoi-like polycrystalline morphologies. The same meshing algorithm is used for the cubic domain. Some statistics about the meshing algorithm are summarized in Tab.(2), which reports the number of degrees of freedom and the number of surface and volume elements of the single crystal meshes involved in the present test, as well as those for the polycrystalline meshes considered in the next section.

26

The cube in Fig.(3) is loaded in uniaxial stress, with uniform tractions act-

Table 2: Statistics about the meshes of the single crystal and polycrystalline domains: d_m is the mesh density parameter; N_e^s is the number of surface elements; $DoFs$ is the number of degrees of freedom for the system in Eq.(27); N_e^v is the number of volume elements. The last column reports the number of volume elements per grain, which is considered as reference to capture the volume field distribution.

morphology	d_m	N_e^s	$DoFs$	N_e^v	N_e^v/N_g
single crystal	2	36	162	46	46
	3	72	288	161	161
	4	150	504	436	436
	5	255	729	836	836
polycrystalline, 10 grains	1	430	3594	562	56
	2	895	6285	1576	158
	3	1811	10131	4097	410
	4	3291	15669	8791	897
	5	5242	22143	16119	1612
polycrystalline, 100 grains (I)	2.5	19902	132369	45704	457
polycrystalline, 100 grains (II)	2.5	18075	122166	40181	402

ing over the top and bottom faces, whereas the lateral faces are traction-free. To avoid the rigid body motion, the technique proposed by Lutz *et al.*[67] is used. Fig.(4a) shows the stress-strain curves of a single crystal cubic domain loaded along the [632] direction for the four considered meshes. The curves are plotted in the strain range 0–2% considering a slip rate sensitivity $n = 50$, and are compared to that obtained for the single crystal centroid. The four meshes replicate the results obtained in Fig.(2d) as uniform strain and stress fields are expected for this configuration. In Fig.(4a), the close-up view shows a comparison between the curves obtained using the surface and the volume inte-
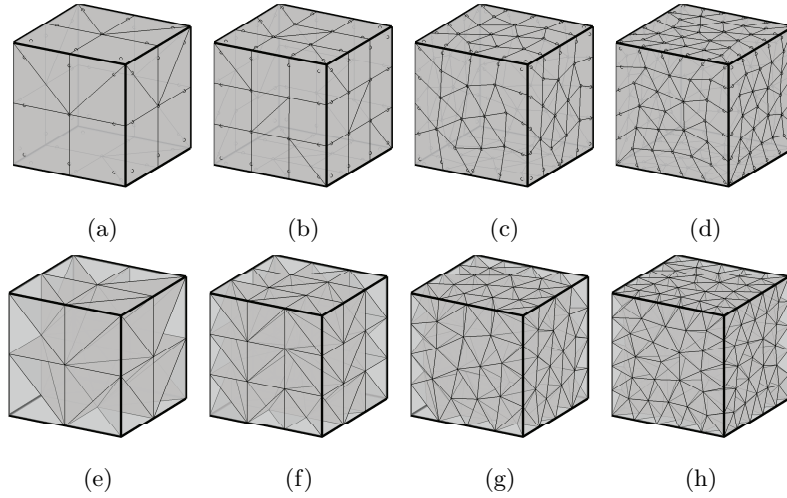
Figure 3: Single crystal surface $(a\text{-}d)$ and volume $(e\text{-}h)$ meshes: (a,e) $d_m = 2$, (b,f) $d_m = 3$, (c,g) $d_m = 4$, (d,h) $d_m = 5$. The small circles in the surface meshes represent the collocation points.

grals of Eqs.(29) and (30). A good match is found among the curves showing a satisfactory accuracy in the integration of the kernels of the boundary integral equations. Finally, Fig.(4b) shows the same response in a smaller strain range, i.e. 0–0.2%.

6.2. Polycrystalline tests

In the present Section, the proposed model is used to simulate the plastic behavior of Cu polycrystalline aggregates. To generate the polycrystalline morphologies, the Neper package [68] is used for its capability of eliminating pathologically small geometrical entities typical of domains subdivided by the Voronoi algorithm, which may induce unnecessarily heavy meshes.

First, a convergence analysis is performed to obtain a proper mesh size ensuring appropriate grains boundary and volume fields resolution and mesh independency of the results. Fig.(5) shows five different meshes $(d_m = 1, 2, ..., 5)$ of a 10-grain aggregate. The statistics about the number of DoFs and the number

28
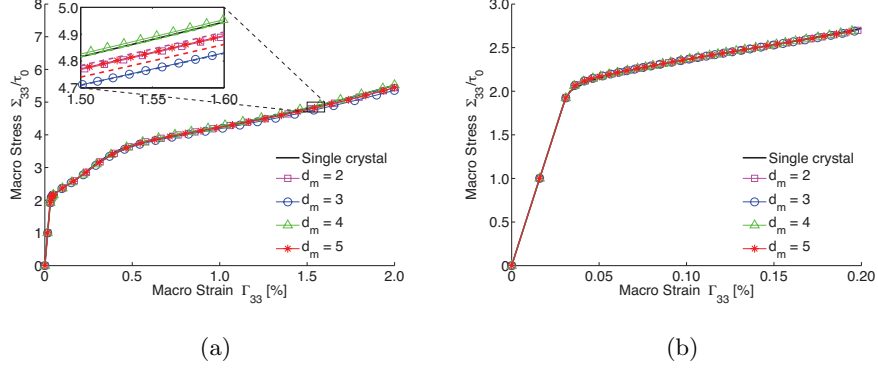
Figure 4: Volume stress average Σ_{33} plotted versus volume strain average Γ_{33} for the four considered meshes of the single crystal loaded along the [632] direction. (a) stress-strain response in the strain range 0–2.0%; the close-up shows the values obtained using the surface integral (solid lines) compared to those obtained using the volume integral (dashed lines). (b) stress-strain response in the range strain 0–0.2%.

of surface and volume elements are summarized in Table (2). The aggregate is loaded in uniaxial tension, with uniform tractions acting over the top and bottom faces, while the lateral faces are traction-free. In this case, to avoid rigid body motion, the elimination of rigid body modes technique is applied to one grain of the aggregate.

Fig.(6a) shows the convergence of the macro stress-strain response of the Cu 10-grain aggregate with respect to the considered meshes. As the model allows to build the surface and the volume meshes separately, Fig.(6a) shows also the macro response obtained combining a surface mesh with a mesh density parameter $d_m = 2$ and a volume mesh with a mesh density parameter $d_m = 3$, which corresponds to the curve labelled with $d_m^s = 2$, $d_m^v = 3$. Fig.(6b) reports the macro-stress error during the loading history between two consecutive mesh refinements defined as:

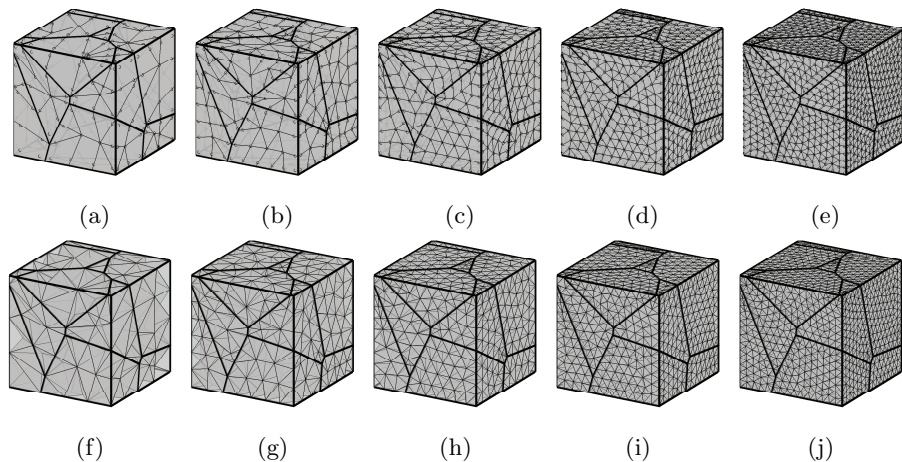$$e(\Sigma_{33}^i, \Sigma_{33}^{i+1}) = 100 \cdot \frac{|\Sigma_{33}^i - \Sigma_{33}^{i+1}|}{\Sigma_{33}^5} \tag{31}$$

29

Figure 5: Surface (a-e) and volume (f-j) meshes of a 10-grain aggregate: (a,f) $d_m = 1$, (b,g) $d_m = 2$, (c,h) $d_m = 3$, (d,i) $d_m = 4$, (e,j) $d_m = 5$. The small circles in the surface meshes represent the collocation points.

where Σ_{33}^i corresponds to the macro stress computed for $d_m = i$.

Fig.(7) shows the deformed configurations of the aggregate for the meshes of Fig.(5) at the last computed step of the load history, i.e. for $\Gamma_{33} = 2\%$. A good convergence is obtained in terms of the grain boundary displacements starting from $d_m = 2$. Fig.(8) and Fig.(9) report the contour plots of the Von Mises stress and cumulative slip fields, respectively. Also in this case, the convergence in terms of the overall behaviour and stress and slip concentration is satisfactorily reached through mesh refinement. It is however noted that a $d_m = 3$ mesh is required to appreciate the fields distribution, likely due to the use of constant volume elements. Considering Table (2), an estimate of the number of volume elements per grain to obtain satisfactory fields distributions within the aggregate appears to be around 400 elements per grain, at least for the present load condition.

The same tensile test is performed on two 100-grain Cu aggregates, in order to evaluate the plastic response of more complex and representative Cu microstructures. The two aggregates are labelled as aggregate (I) and (II). Fig.(10a) and
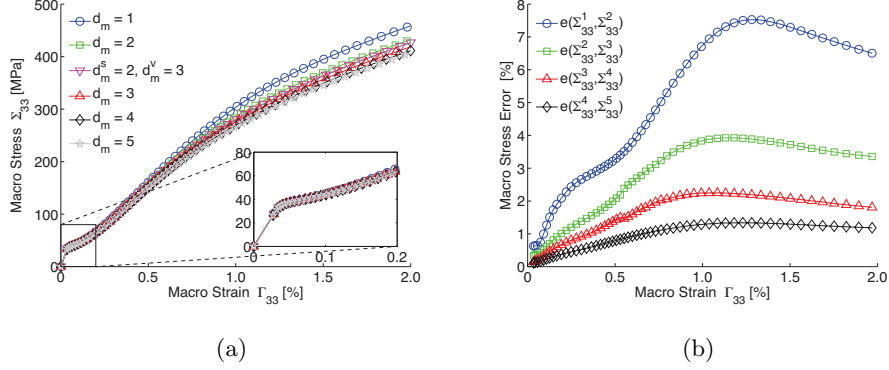
30

Figure 6: Volume stress average Σ_{33} versus volume strain average Γ_{33} for the considered meshes of the 10-grain aggregate. (a) Stress-strain response in the strain range 0–2.0%; the close-up shows the values obtained in the strain range 0–0.2%. (b) Error between two consecutive mesh refinements.

Fig.(10d) show the microstructures (I) and (II), respectively. Figs.(10b,e) show the corresponding surface meshes, whereas Figs.(10c,f) show the volume meshes. The meshes are built using a mesh density parameter that ensures an average number of 400 volume elements per grain, see Table (2), which represents a good tradeoff between solution accuracy and number of DoFs. Fig.(11a) shows the macro stress-strain behaviour of the two aggregates, which is qualitatively similar to that obtained for the 10-grain aggregate. The insert of the figure reports a close-up view of the macro response in the range $0 \div 1.5\%$, showing the transition from the linear to the plastic slip behaviour. By comparing the response of the two microstructures, it can be noted that an aggregate with 100 grains is satisfactorily representative for polycrystalline Cu undergoing small strains crystal plasticity. The solid line in Fig.(11a) represents the linear response of the microstructure whose averaged stiffness is calculated using the Hashin-Shtrikman bounds [69], whereas the dashed line reports the response of the aggregate using the Berveiller and Zaoui (BZ) model [70]. It can be noted that the BZ model and the present model agree very well with respect to the
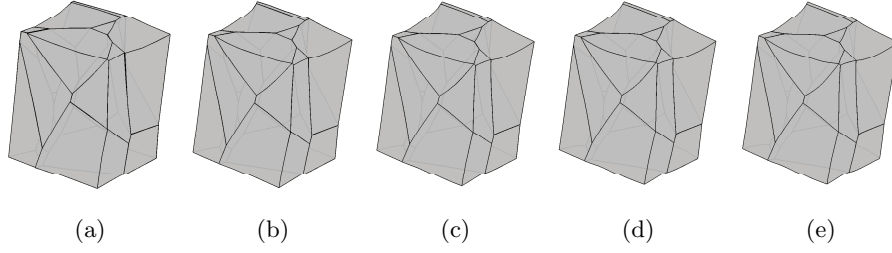
31

(a) (b) (c) (d) (e)

Figure 7: Deformed shape for the five considered meshes of the 10-grain poly-crystalline copper aggregate subjected to tensile load at the last computed step ($\Gamma_{33} = 2\%$). Figs.(a) to (e) correspond to the (a) to (e) surface meshes and (f) to (j) volume meshes of Fig.(5), respectively.

elastic to plastic behavior transition. On the other hand, the BZ model provides values of stress higher than the present model, but this appears consistent with Barbe *et al.* [17], who reported an overestimate with respect to FEM as well. Fig.(11b) shows the averaged stress-strain behavior of each of the 100 grains of the aggregates, obtained using Eqs.(29) and (30) where the integration is performed over the boundary of *each* grain. Eventually, Fig.(12a) and Fig.(13a) report the contour plots of the Von Mises stress and cumulative slip fields, respectively, over the external boundary of the aggregate (I), whereas Fig.(12b) and Fig.(13b) report the same contour plots for a section of the aggregate giving an insight of the internal volume fields distribution.

In conclusion, a comparison with the homogenisation results obtained using the crystal plasticity finite element method is presented. The reference is the work by Barbe *et al.*[17], where the response of polycrystalline aggregates at small strains is studied using FEM. In their work, the authors employ the model proposed by Méric and Cailletaud [71], which is briefly recalled in Appendix B for the sake of completeness.

Fig.(14) shows the comparison between the results obtained using the FEM and those obtained from the presented formulation. The FEM aggregate consists of 200 grains with random crystallographic orientations, discretized using a struc-
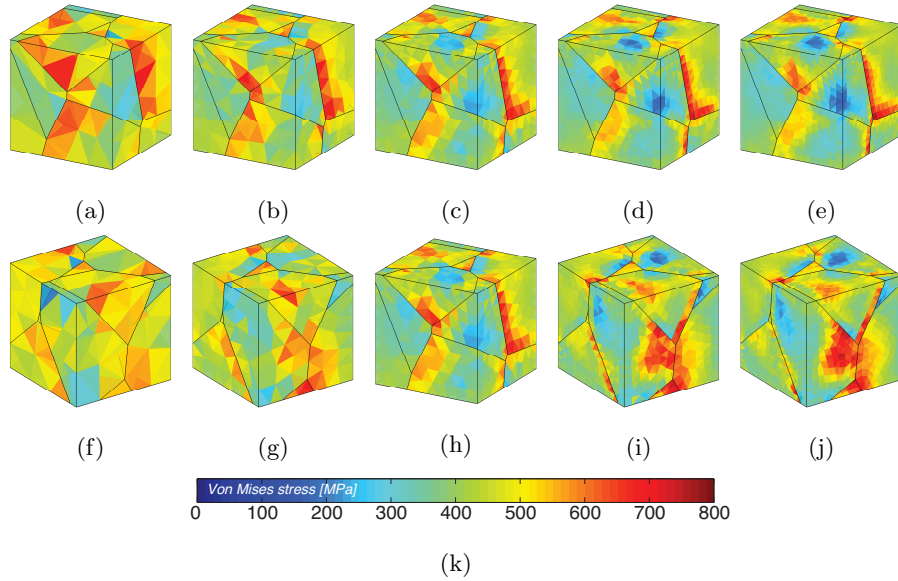
32

Figure 8: Von Mises stress contour plots for the 10-grain polycrystalline copper aggregate subjected to tensile load at the last computed step ($\Gamma_{33} = 2\%$). Figs.(*a-e*) and Figs.(*h-j*) correspond to two different views of the aggregate. (*k*) Colormap (to interpret the colour scale, the reader is referred to the web version of the article).

590   tured mesh, and whose elastic and plastic properties are listed in Tab.(3). The elastic, slip rate and hardening constants are taken from [17], whereas the interaction hardening moduli from the work of Gerard *et al.*[72], who adopted such coefficients based on the work on dislocation dynamic simulations for FCC crystals of Devincre *et al.* [73].

595   In Fig.(14a), the FEM points, denoted by small circles, indicate the response of a polycrystalline aggregate subjected to iso-volumic boundary conditions as described in [17]. Fig.(14b) shows the averaged lateral stress. The aggregate is loaded along the x_3 direction, so that the axial stress and strain correspond to the averaged macro-stress Σ_{33} and macro-strain Γ_{33}, respectively. The lateral

600   stresses correspond to the averaged macro-stresses Σ_{11} and Σ_{22}. The results shown in Fig.(14) are reported for the strain range $0 \div 0.6\%$. However, in this
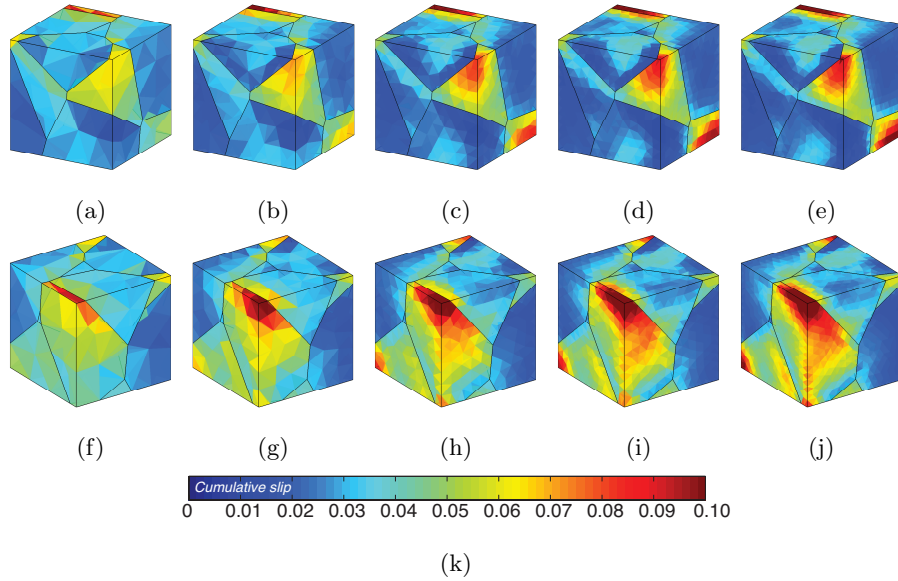
Figure 9: Cumulative slip contour plots of the 10-grain polycrystalline copper aggregate subjected to tensile load at the last computed step ($\Gamma_{33} = 2\%$). Figs.(a-e) and Figs.(h-j) correspond to two different views of the aggregate. (k) Colormap (to interpret the colour scale, the reader is referred to the web version of the article).

strain range it is still possible to assess the capabilities of the present formulation, as the plastic behaviour of the polycrystalline aggregate is well developed. The presented results highlight a satisfactory agreement between the results of the present formulation and those reported in the literature.

7. Discussion and possible developments

The presented formulation addresses, for the first time, crystal plasticity in a boundary element framework, both for single crystals and crystal aggregates. From this point of view, it may be interesting to note that, while the possibility of using boundary elements for crystal plasticity is mentioned in the very
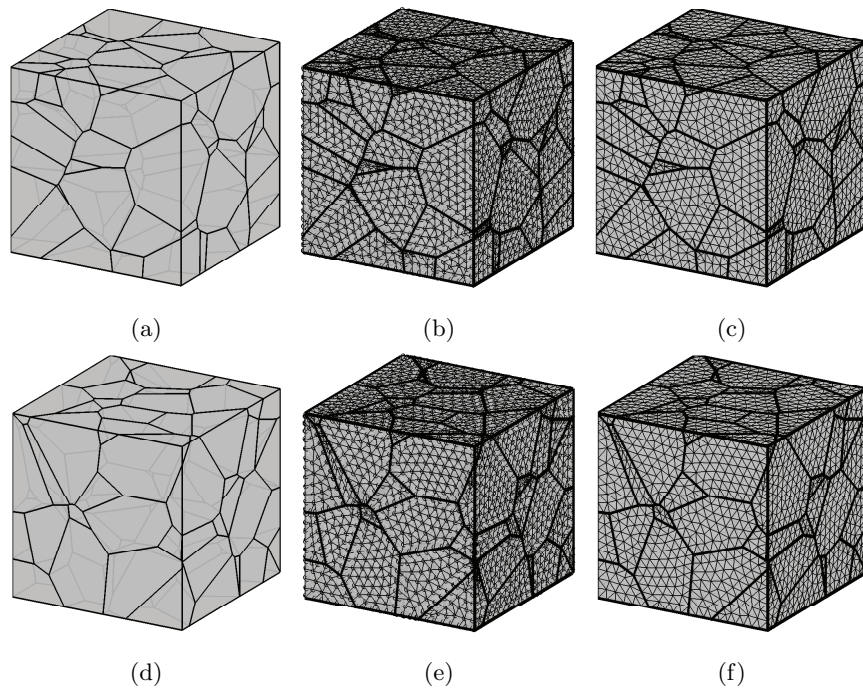
34

Figure 10: (a,d) 100-grain polycrystalline microstructure (I) and (II), respectively; corresponding surface (b,e) and volume (c,f) meshes.

exhaustive review [2], no reference is provided to crystal plasticity boundary elements papers.

The salient feature of the method is its expression in terms of grain-boundary variables only, namely in terms of intergranular displacements and tractions. In previous applications, see e.g. [47, 48, 50], this aspect ensured *simplification* in data preparation, as only meshing of the inter-granular interfaces was required, and a *reduction* in the number of DoFs for the analysis, particularly appreciated in polycrystalline problems. In crystal plasticity applications, the data preparation simplification with respect to other techniques is lost, due to the need of meshing the grains interior volume; however, the system order reduction is maintained, as *the volume mesh does not carry additional degrees of freedom*. The volume mesh is in fact only used to compute the plastic contribution on the
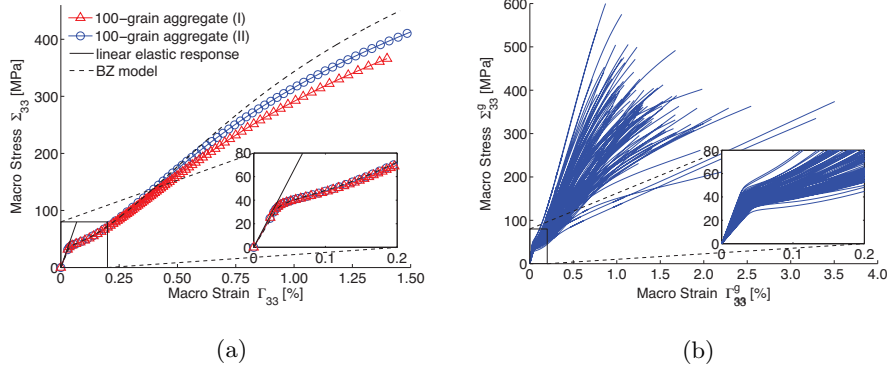
35

Figure 11: (*a*) Volume stress average Σ_{33} versus volume strain average Γ_{33} for the two 100-grain aggregates; the solid line represents the linear elastic behaviour computed using the Hashin-Shtrikman bounds [69]; (*b*) Averaged stress-strain behaviour for *each* constituent grain of the aggregate (I).

right-hand side of Eq.(27), while *the number of degrees of freedom with respect*
₆₂₅ *to the purely elastic case remains unchanged.* Additionally, it is worth noting that the plastic accumulation just modifies the right-hand side of Eq.(27): such circumstance is particularly advantageous in terms of numerical solution, as the factorization of the coefficient matrix in the left-hand side of Eq.(27) is performed just once and used throughout the analysis, thus ensuring numerical
₆₃₀ effectiveness.

Although the proposed scheme allows a considerable reduction in the number of DoFs with respect to other volume discretization schemes, the solution of system (27) still represents a formidable computational task, especially in the polycrystalline case, due to the fact that the numerical blocks associated to each
₆₃₅ grain in the boundary integral scheme are fully populated. For such reason, at least in the present implementation, the typical computation time is longer than the typical times with CPFEMs or Fast Fourier Transform based formulations, see e.g. Ref.[74]. An interesting direction of further investigation, from this point of view, could be related to the use of fast multipoles [75] or hierarchical
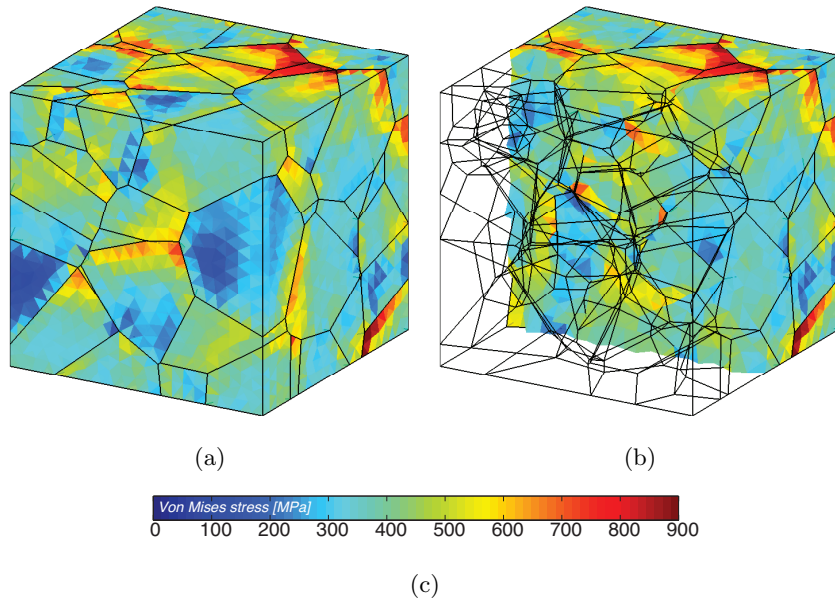
36

Figure 12: Von Mises stress contour plots for the 100-grain polycrystalline copper aggregate (I) at the last computed step ($\Gamma_{33} = 1.5\%$); (b) Section of the aggregate; (c) Colormap (to interpret the colour scale, the reader is referred to the web version of the article).

matrices [76, 64, 65, 77, 78] in conjunction with iterative solvers to reduce the computational time and further compress the storage memory requirements of the proposed framework . On the other hand, the implementation of effective rate-independent schemes [7, 79, 80], could speed up the iterative convergence of the crystal plastic analysis, avoiding the numerical *stiffness*, and the associated computational costs, associated to high values of the rate sensitivity n appearing in Eq.(B.1).

In the developed model, a phenomenological description of crystal plasticity has been adopted. However, the model offers flexibility and could be coupled with more sophisticated crystal plasticity laws, included physically based approaches. Another natural extension could be the introduction of different models of grain interfaces, which at the moment are modelled as perfect and remain intact dur-
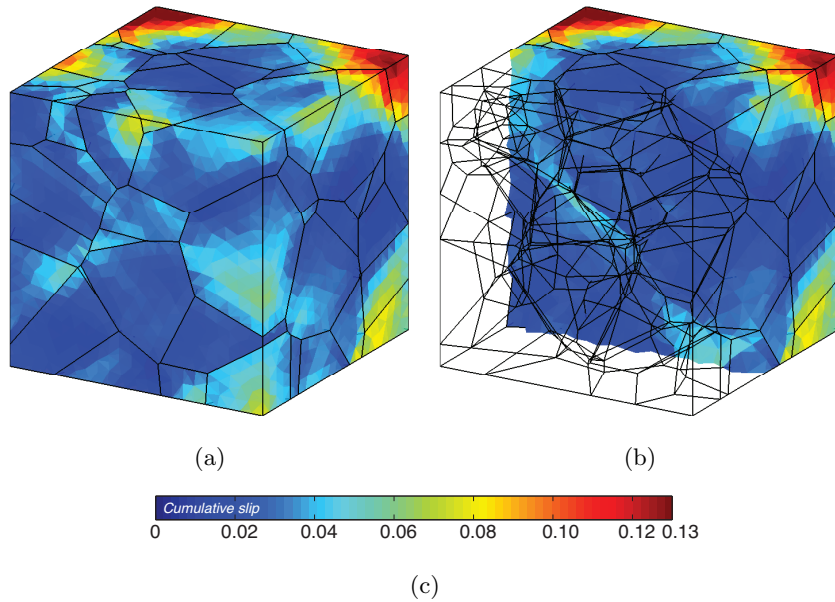
Figure 13: Cumulative slip contour plots for the 100-grain polycrystalline copper aggregate (I) at the last computed step ($\Gamma_{33} = 1.5\%$); (b) Section of the aggregate; (c) Colour map (to interpret the colorscale, the reader is referred to the web version of the article).

ing the loading history. Sliding, separation and contact could be included within the formulation by suitably redefining the interface equations in (27).

The presented formulation has also some limitations, which provide input for
₆₅₅ further investigation. First of all, the formulation is confined within the framework of *small strains*, so that *finite* lattice rotations are not taken into account. For this reason, applications to *texture evolution* problems are not currently possible. In fact, the present formulation is based on an *elasto-plastic* analysis, while crystal plastic finite element formulations for texture evolution are
₆₆₀ often based on *rigid-plastic* approaches, where the initial elastic behaviour is neglected [12, 58]. The extension of the developed grain-boundary framework to finite strains and the inclusion of finite rotations is not a trivial task and poses considerable research challenges that are left as future task.

38

Table 3: Material parameters for FEM-BEM comparison. The elastic, slip rate and hardening constants are taken from [17], whereas the interaction hardening moduli from [72].

elastic behavior	$E = 169$ GPa, $\nu = 0.3$
slip rate constants	$K = 10$ MPa s$^{1/n}$, $n = 25$
hardening constants	$R_0 = 111$ MPa, $Q = 35$ MPa, $b = 7$
hardening moduli	self hardening, $h_0 = 1.0$ coplanar interaction, $h_1 = 1.0$ Hirth lock, $h_2 = 0.2$ collinear interaction, $h_3 = 90.0$ glissile junction, $h_4 = 3.0$ Lomer lock, $h_5 = 2.5$

8. Conclusions

A boundary element formulation for small strains crystal plasticity has been presented the first time. The method, based on the use of grain-boundary integral equations for the anisotropic elasto-plastic problem, is formulated in terms of boundary (inter-granular) displacements and tractions, which play the role of primary variables, thus allowing a considerable reduction in the number of DoFs with respect to other volume discretization techniques. The scheme has been implemented both for single crystals and polycrystalline aggregates and a general rate-dependent scheme has been used in the proposed incremental/iterative grain-boundary crystal plasticity algorithm. Several numerical tests have been performed to assess the accuracy and robustness of the method and the results confirm the potential of the developed tool. Although the still high computational costs associated with the analysis of general plastic polycrystalline problems call for further developments and refinements, the presented framework
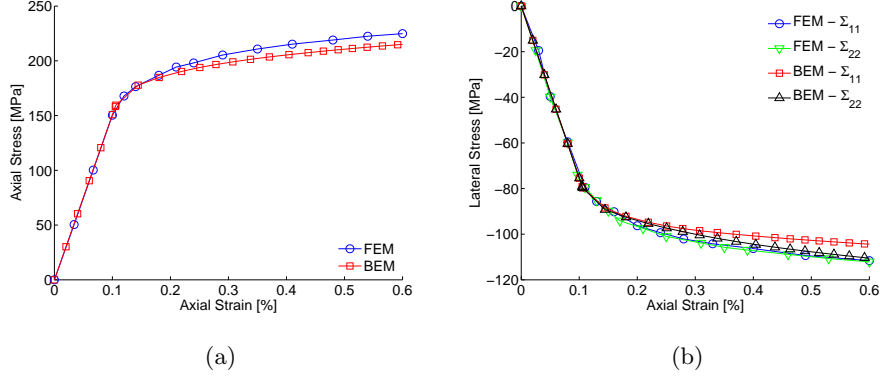
Figure 14: Comparison between FEM results [17] and the present BEM for-
mulation. (a) Macro stress-strain behaviour of a polycrystalline aggregate sub-
jected to iso-volumic boundary conditions; (b) Lateral macro-stresses versus
axial macro-strain.

provides an alternative tool for the analysis of this class of problems.

Appendix A. Anisotropic Green's functions

Defined the unit vector $\boldsymbol{b} = (\boldsymbol{x} - \boldsymbol{y})/\|\boldsymbol{x} - \boldsymbol{y}\|$ in the direction connecting
the collocation point $\boldsymbol{x}$ with the integration point $\boldsymbol{y}$, the anisotropic Green's
function can be written

$$G_{ij} = \frac{1}{8\pi^2 r} \int_0^{2\pi} M_{ij}^{-1}\left[\boldsymbol{z}(\varphi)\right] d\varphi \qquad M_{ij}\left[\boldsymbol{z}(\varphi)\right] = C_{ipjq} z_p(\varphi) z_q(\varphi) \qquad (A.1)$$

where $r = \|\boldsymbol{x} - \boldsymbol{y}\|$, $\boldsymbol{z}$ is a unit vector lying on the plane Π perpendicular to
$\boldsymbol{b}$, $\boldsymbol{z} \cdot \mathbf{b} = 0$, whose position is given in terms of the angle φ with respect to a

40

reference axis on Π, and C_{ipjq} are the components of the stiffness tensor. The integration in Eq.(A.1) is the performed along a unit circle lying on the plane Π.

The kernels appearing in the boundary integral equations appearing in the formulation can all be expressed in terms of the Green's functions G_{ij} and their first and second derivatives, which are given by

$$\frac{\partial G_{ij}}{\partial y_p} = \frac{1}{4\pi^2 r^2} \int_0^\pi (-b_p M_{ij}^{-1} + z_p F_{ij}) d\varphi \tag{A.2}$$

$$\frac{\partial^2 G_{ij}}{\partial y_p \partial y_q} = \frac{1}{4\pi^2 r^3} \int_0^\pi [2 b_p b_q M_{ij}^{-1} - 2(z_p b_q + z_q b_p) F_{ij} + z_p z_q A_{ij}] d\varphi \tag{A.3}$$

where the integration is still performed on the plane Π and

$$F_{ij} = C_{mnpq} M_{im}^{-1} M_{pj}^{-1} (z_n b_q + z_q b_n) \tag{A.4}$$

$$A_{ij} = C_{mnpq}[(z_n b_q + z_q b_n)(F_{im} M_{pj}^{-1} + M_{im}^{-1} F_{pj}) - 2 M_{im}^{-1} M_{pj}^{-1} b_n b_q] \tag{A.5}$$

Appendix B. Flow rules and hardening laws

In the present work two different crystal plasticity phenomenological frameworks have been used in the performed numerical tests: the model by Bassani and Wu [12] and the model by Méric and Cailletaud [71].

Bassani and Wu used as flow rule a power law of the form

$$\dot{\gamma}^\alpha = \dot{\gamma}_0^\alpha \left| \frac{\tau^\alpha}{\tau_c^\alpha} \right|^n sgn(\tau^\alpha) \qquad \forall \alpha = 1, \cdots, N_s \tag{B.1}$$

where $\dot{\gamma}_0^\alpha$ and n are material parameters known as *reference shear rate* and *rate sensitivity of slip* respectively, while τ_c^α is the evolving critical stress. Eq.(B.1) describes, in general, a rate–dependent phenomenon in which all the slip systems are always *active* with a specific slip rate $\dot{\gamma}^\alpha$, as long as the corresponding resolved shear stress is non-zero, so that no distinction is made between *active* and *inactive* slip systems. It can be demonstrated that when $n \to \infty$ the formulation becomes rate–independent.

41

They also expressed the *hardening laws*, i.e. the evolution of τ_c^α with respect to the material state and evolution, as

$$\dot{\tau}_c^\alpha = \sum_{\beta=1}^{N_s} h_{\alpha\beta} \left| \dot{\gamma}^\beta \right| \qquad \forall \alpha = 1, \cdots, N_s \tag{B.2}$$

where the *self hardening* moduli $h_{\alpha\alpha}$ and the *latent hardening* moduli $h_{\alpha\beta}$ were expressed as

$$h_{\alpha\alpha} = \left[h_s + (h_0 - h_s) \operatorname{sech}^2 \left(\frac{h_0 - h_s}{\tau_s - \tau_0^\alpha} \cdot \gamma^\alpha \right) \right] \cdot \left[1 + \sum_{\beta \neq \alpha} f_{\alpha\beta} \tanh \left(\frac{\gamma^\beta}{\gamma_p} \right) \right] \tag{B.3}$$

$$h_{\alpha\beta} = q \cdot h_{\alpha\alpha} \qquad \beta \neq \alpha \tag{B.4}$$

where: h_0 is the initial hardening modulus; h_s is the hardening modulus during easy glide within stage I hardening; τ_s is the stage I reference stress, where large plastic flow initiates; $\tau_0^\alpha = \tau_c^\alpha(0)$ is the initial critical resolved shear stress on the α-th slip system; $\gamma^\alpha = \int_t |\dot{\gamma}^\alpha| dt$; γ_p is the amount of slip after which the interaction between slip systems reaches the peak strength; $f_{\alpha\beta}$ is a specific slip interaction strength; q is a constant latent hardening factor. The model by Bassani and Wu has been implemented in several FEM formulations, also for polycrystalline micromechanics [81, 82], often using the implementation developed by Huang [58].

On the other hand, neglecting the kinematic hardening, Méric and Cailletaud represented the slip rate $\dot{\gamma}^\alpha$ of the α-th slip system using the following flow rule

$$\dot{\gamma}^\alpha = \left\langle \frac{|\tau^\alpha| - \tau_c^\alpha}{K} \right\rangle^n sgn\left(\tau^\alpha\right) \tag{B.5}$$

where $\langle \cdot \rangle = \max(0, \cdot)$ and K and n are material parameters. In addition, in their model, the hardening law, which comprises self and latent hardening through the hardening moduli $h_{\alpha\beta}$, has the form

$$\tau_c^\alpha = R_0 + Q \sum_{\beta=1}^{N_s} h_{\alpha\beta} \left[1 - \exp(-b|\gamma^\beta|) \right] \qquad \forall \alpha = 1, \cdots, N_s \tag{B.6}$$

where R_0 is the initial critical resolved shear stress; Q is a material parameter that, multiplied by the hardening modulus $h_{\alpha\beta}$, represents the maximal increase

42

of the critical shear stress on the α-th slip system due to the slip in the β-th

730   system; $R_0 + Q \sum_\beta h_{\alpha\beta}$ represents the maximum, or *saturated*, value that the

critical shear stress on the α-th slip system can reach; eventually, b is a material

parameter that governs the exponential saturation law.

References

735   [1] I. Benedetti, F. Barbe, Modelling polycrystalline materials: An overview
of three-dimensional grain-scale mechanical models, Journal of Multiscale
Modelling 05 (01) (2013) 1350002. `doi:10.1142/S1756973713500029`.

[2] F. Roters, P. Eisenlohr, L. Hantcherli, D. Tjahjanto, T. Bieler, D. Raabe,
Overview of constitutive laws, kinematics, homogenization and multiscale methods in crystal plasticity fi

740   Acta   Materialia   58   (4)   (2010)   1152   –   1211.
`doi:http://dx.doi.org/10.1016/j.actamat.2009.10.058`.
URL `http://www.sciencedirect.com/science/article/pii/S1359645409007617`

[3] A. Needleman, Computational mechanics at the mesoscale, Acta Materialia
48 (1) (2000) 105 – 124.

745   [4] J. Rice, Inelastic constitutive relations for solids: An internal-variable theory and its application to metal
Journal of the Mechanics and Physics of Solids 19 (6) (1971) 433 – 455.
`doi:http://dx.doi.org/10.1016/0022-5096(71)90010-X`.
URL `http://www.sciencedirect.com/science/article/pii/002250967190010X`

[5] D.   Peirce,   R.   Asaro,   A.   Needleman,

750   Material rate dependence and localized deformation in crystalline solids,
Acta   Metallurgica   31   (12)   (1983)   1951   –   1976.
`doi:http://dx.doi.org/10.1016/0001-6160(83)90014-7`.
URL `http://www.sciencedirect.com/science/article/pii/0001616083900147`

[6] X.   Ling,   M.   F.   Horstemeyer,   G.   P.   Potirniche,

755   On the numerical implementation of 3d rate-dependent single crystal plasticity formulations,

International Journal for Numerical Methods in Engineering 63 (4) (2005) 548–568. `doi:10.1002/nme.1289`.
URL `http://dx.doi.org/10.1002/nme.1289`

[7] L. Anand, M. Kothari, A computational procedure for rate-independent crystal plasticity, Journal of the Mechanics and Physics of Solids 44 (4) (1996) 525 – 558. `doi:http://dx.doi.org/10.1016/0022-5096(96)00001-4`.
URL `http://www.sciencedirect.com/science/article/pii/0022509696000014`

[8] C. Miehe, J. Schröder, A comparative study of stress update algorithms for rate-independent and rate-dependent crystal plasticity, International Journal for Numerical Methods in Engineering 50 (2) (2001) 273–298.

[9] P. Wu, K. Neale, E. V. der Giessen, Simulation of the behaviour of {FCC} polycrystals during reversed torsion, International Journal of Plasticity 12 (9) (1996) 1199 – 1219. `doi:http://dx.doi.org/10.1016/S0749-6419(96)00048-4`.
URL `http://www.sciencedirect.com/science/article/pii/S0749641996000484`

[10] R. Asaro, A. Needleman, Texture development and strain hardening in rate dependent polycrystals, Acta Metallurgica 33 (6) (1985) 923 – 953. `doi:http://dx.doi.org/10.1016/0001-6160(85)90188-9`.
URL `http://www.sciencedirect.com/science/article/pii/0001616085901889`

[11] S. Harren, T. C. Lowe, R. J. Asaro, A. Needleman, Analysis of large-strain shear in rate-dependent face-centred cubic polycrystals: Correlation of micro- and macromechanics, Philosophical Transactions of the Royal Society of London A: Mathematical, Physical and Engineering Sciences 328 (1600) (1989) 443–500. `doi:10.1098/rsta.1989.0048`.

[12] J. L. Bassani, T.-Y. Wu, Latent hardening in single crystals ii. analytical characterization and predictions, Proceedings of the Royal Society of London. Series A: Mathematical and Physical Sciences 435 (1893) (1991) 21–41.

[13] S. Kalidindi, C. Bronkhorst, L. Anand, Crystallographic texture evolution in bulk deformation processing of {FCC} metals, Journal of the Mechanics and Physics of Solids 40 (3) (1992) 537 – 569. doi:http://dx.doi.org/10.1016/0022-5096(92)80003-9. URL http://www.sciencedirect.com/science/article/pii/0022509692800039

[14] M. Kovač, L. Cizelj, Modeling elasto-plastic behavior of polycrystalline grain structure of steels at mesoscopic level, Nuclear engineering and design 235 (17) (2005) 1939–1950.

[15] G. Sarma, B. Radhakrishnan, T. Zacharia, Finite element simulations of cold deformation at the mesoscale, Computational Materials Science 12 (2) (1998) 105 – 123. doi:http://dx.doi.org/10.1016/S0927-0256(98)00036-6. URL http://www.sciencedirect.com/science/article/pii/S0927025698000366

[16] S. Quilici, G. Cailletaud, FE simulation of macro-, meso- and micro-scales in polycrystalline plasticity, Computational Materials Science 16 (14) (1999) 383 – 390. doi:http://dx.doi.org/10.1016/S0927-0256(99)00081-6. URL http://www.sciencedirect.com/science/article/pii/S0927025699000816

[17] F. Barbe, L. Decker, D. Jeulin, G. Cailletaud, Intergranular and intragranular behavior of polycrystalline aggregates. Part 1: F.E. model, International Journal of Plasticity 17 (2001) 513–536.

[18] F. Barbe, S. Forest, G. Cailletaud, Intergranular and intragranular behavior of polycrystalline aggregates. Part 2: Results, International Journal of Plasticity 17 (2001) 537–563.

[19] C. Fahrat, F.-X. Roux, Implicit Parallel Processing in Structural Mechanics, Computational Mechanics Advances 2 (1).

[20] O. Diard, S. Leclercq, G. Rousselier, G. Cailletaud, Evaluation of finite element based analysis of 3D multicrystalline aggregates plasticity: Application to cr International Journal of Plasticity 21 (4) (2005) 691 – 722.

doi:http://dx.doi.org/10.1016/j.ijplas.2004.05.017.

URL http://www.sciencedirect.com/science/article/pii/S0749641904000774

[21] G. Sarma, B. Radhakrishnan, Modeling microstructural effects on the evolution of cube texture during ho

Materials Science and Engineering: A 385 (12) (2004) 91 – 104.

doi:http://dx.doi.org/10.1016/j.msea.2004.06.007.

URL http://www.sciencedirect.com/science/article/pii/S0921509304008111

[22] A. Zeghadi, S. Forest, A.-F. Gourgues, O. Bouaziz,

Ensemble averaging stress-strain fields in polycrystalline aggregates with a constrained surface microstru

Philosophical Magazine 87 (8-9) (2007) 1425–1446.

arXiv:http://www.tandfonline.com/doi/pdf/10.1080/14786430601009517,

doi:10.1080/14786430601009517.

URL http://www.tandfonline.com/doi/abs/10.1080/14786430601009517

[23] E. Héripré, M. Dexet, J. Crépin, L. Gélébart,

A. Roos, M. Bornert, D. Caldemaison,

Coupling between experimental measurements and polycrystal finite element calculations for micromecha

International Journal of Plasticity 23 (9) (2007) 1512 – 1539.

doi:http://dx.doi.org/10.1016/j.ijplas.2007.01.009.

URL http://www.sciencedirect.com/science/article/pii/S074964190700006X

[24] A. Musienko, A. Tatschl, K. Schmidegg, O. Kolednik, R. Pippan, G. Cail-
letaud, Three-dimensional finite element simulation of a polycrystalline
copper specimen, Acta Materialia 55 (2007) 4121–4136.

[25] C. Zhang, H. Li, P. Eisenlohr, W. Liu, C. Boehlert, M. Crimp, T. Bieler,
Effect of realistic 3d microstructure in crystal plasticity finite element anal-
ysis of polycrystalline ti-5al-2.5 sn, International Journal of Plasticity 69
(2015) 21–35.

[26] C. Pinna, Y. Lan, M. Kiu, P. Efthymiadis, M. Lopez-Pedrosa, D. Farru-
gia, Assessment of crystal plasticity finite element simulations of the hot
deformation of metals from local strain and orientation measurements, In-
ternational Journal of Plasticity 73 (2015) 24–38.

46

[27] F. Barbe, R. Quey, A numerical modelling of 3D polycrystal-to-polycrystal diffusive phase transformation
International Journal of Plasticity 27 (6) (2011) 823 – 840.
doi:http://dx.doi.org/10.1016/j.ijplas.2010.09.008.
URL http://www.sciencedirect.com/science/article/pii/S0749641910001348

[28] Y. Schneider, A. Bertram, T. Böhlke, C. Hartig,
Plastic deformation behaviour of Fe-Cu composites predicted by 3D finite element simulations,
Computational Materials Science 48 (3) (2010) 456 – 465.
doi:http://dx.doi.org/10.1016/j.commatsci.2010.01.005.
URL http://www.sciencedirect.com/science/article/pii/S0927025610000157

[29] Y. Schneider, A. Bertram, T. Böhlke, Three-dimensional simulation of local
and global behaviour of αFe-Cu composites under large plastic deformation,
Technische Mechanik 33 (1) (2013) 34–51.

[30] I. Simonovski, L. Cizelj, Cohesive zone modeling of intergranular cracking in polycrystalline aggregates,
Nuclear Engineering and Design 283 (0) (2015) 139 – 147, sI:NENE 2013.
doi:http://dx.doi.org/10.1016/j.nucengdes.2014.09.041.
URL http://www.sciencedirect.com/science/article/pii/S0029549314005548

[31] C. Robert, C. Mareau, A comparison between different numerical methods for the modeling of polycrystal
Computational Materials Science 103 (0) (2015) 134 – 144.
doi:http://dx.doi.org/10.1016/j.commatsci.2015.03.028.
URL http://www.sciencedirect.com/science/article/pii/S0927025615001901

[32] K. Zhang, B. Holmedal, O. S. Hopperstad, S. Dumoulin, J. Gawad,
A. Van Bael, P. Van Houtte, Multi-level modelling of mechanical anisotropy
of commercial pure aluminium plate: crystal plasticity models, advanced
yield functions and parameter identification, International Journal of Plas-
ticity 66 (2015) 3–30.

[33] W. Zeng, J. Larsen, G. Liu, Smoothing technique based crystal plasticity
finite element modeling of crystalline materials, International Journal of
Plasticity 65 (2015) 250–268.

[34] J.-B. Kim, J. W. Yoon, Necking behavior of aa 6022-t4 based on the crystal plasticity and damage models, International Journal of Plasticity 73 (2015) 3–23.

[35] H. Abdolvand, M. R. Daymond, C. Mareau, Incorporation of twinning into a crystal plasticity finite element model: evolution of lattice strains and texture in zircaloy-2, International Journal of Plasticity 27 (11) (2011) 1721–1738.

[36] H. Wang, P. Wu, J. Wang, C. Tomé, A crystal plasticity model for hexagonal close packed (hcp) crystals including twinning and de-twinning mechanisms, International Journal of Plasticity 49 (2013) 36–52.

[37] H. Lim, C. R. Weinberger, C. C. Battaile, T. E. Buchheit, Application of generalized non-schmid yield law to low-temperature plasticity in bcc transition metals, Modelling and Simulation in Materials Science and Engineering 21 (4) (2013) 045015.

[38] H. Lim, J. Carroll, C. Battaile, T. Buchheit, B. Boyce, C. Weinberger, Grain-scale experimental validation of crystal plasticity finite element simulations of tantalum oligocrystals, International Journal of Plasticity 60 (2014) 1–18.

[39] C. Brebbia, J. Telles, L. Wrobel, Boundary element techniques, Springer-Verlag, 1984.

[40] P. Banerjee, The boundary element methods in engineering, McGraw-Hill, 1994, (pp. 177–188).

[41] M. H. Aliabadi, The boundary element method: applications in solids and structures., Vol. 2, John Wiley & Sons Ltd, England, 2002.

[42] M. Bonnet, S. Mukherjee, Implicit {BEM} formulations for usual and sensitivity problems in elasto-plasti International Journal of Solids and Structures 33 (30) (1996) 4461 – 4480. doi:http://dx.doi.org/10.1016/0020-7683(95)00279-0. URL http://www.sciencedirect.com/science/article/pii/0020768395002790

[43] A. P. Cisilino, M. H. Aliabadi, J. L. Otegui, A three-dimensional boundary element formulation for the elastoplastic analysis of cracked bodies, International Journal for Numerical Methods in Engineering 42 (2) (1998) 237–256. `doi:10.1002/(SICI)1097-0207(19980530)42:2<237::AID-NME359>3.0.CO;2-6.` URL `http://dx.doi.org/10.1002/(SICI)1097-0207(19980530)42:2<237::AID-NME359>3.0.CO;2-6`

[44] A. Benallal, C. A. Fudoli, W. S. Venturini, An implicit bem formulation for gradient plasticity and localization phenomena, International Journal for Numerical Methods in Engineering 53 (8) (2002) 1853–1869. `doi:10.1002/nme.365.` URL `http://dx.doi.org/10.1002/nme.365`

[45] V. Mallardo, C. Alessandri, Arc-length procedures with {BEM} in physically nonlinear problems, Engineering Analysis with Boundary Elements 28 (6) (2004) 547 – 559. `doi:http://dx.doi.org/10.1016/j.enganabound.2003.11.002.` URL `http://www.sciencedirect.com/science/article/pii/S095579970300198X`

[46] V. Mallardo, Integral equations and nonlocal damage theory: a numerical implementation using the bdem, International journal of fracture 157 (1-2) (2009) 13–32.

[47] I. Benedetti, M. Aliabadi, A three-dimensional grain boundary formulation for microstructural modeling of polycrystalline materials, Computational Materials Science 67 (2013) 249–260.

[48] I. Benedetti, M. Aliabadi, A three-dimensional cohesive-frictional grain-boundary micromechanical model for intergranular degradation and failure in polycrystalline materials, Computer Methods in Applied Mechanics and Engineering 265 (2013) 36–62.

[49] I. Benedetti, M. Aliabadi, Multiscale modelling of polycrystalline materials: a boundary element approach to material degradation and fracture, Computer Methods in Applied Mechanics and Engineering 289 (0) (2015) 429 – 453.

49

[50] V. Gulizzi, A. Milazzo, I. Benedetti, An enhanced grain-boundary framework for computational homogenization and micro-cracking simulatio Computational Mechanics (2015) 1–21doi:10.1007/s00466-015-1192-8.
URL http://dx.doi.org/10.1007/s00466-015-1192-8

[51] T. Mura, N. Kinoshita, Green's functions for anisotropic elasticity, Physica status solidi (b) 47 (2) (1971) 607–618.

[52] K. Malen, A unified six-dimensional treatment of elastic green's functions and dislocations, Physica status solidi (b) 44 (2) (1971) 661–672.

[53] D. Barnett, The precise evaluation of derivatives of the anisotropic elastic green's functions, Physica status solidi (b) 49 (2) (1972) 741–748.

[54] N. Schclar, P. Partridge, 3d anisotropic elasticity with bem using the isotropic fundamental solution, Engineering analysis with boundary elements 11 (2) (1993) 137–144.

[55] N. A. Schclar, Anisotropic analysis using boundary elements, Vol. 20 of Topics in Engineering, Computational Mechanics Publications, 1994.

[56] X.-W. Gao, T. G. Davies, An effective boundary element algorithm for 2d and 3d elastoplastic problems, International Journal of Solids and Structures 37 (36) (2000) 4987 – 5008.
doi:http://dx.doi.org/10.1016/S0020-7683(99)00188-2.
URL http://www.sciencedirect.com/science/article/pii/S0020768399001882

[57] J. Telles, C. Brebbia, The boundary element method in plasticity, Applied Mathematical Modelling 5 (4) (1981) 275–281.

[58] Y. Huang, A User-material Subroutine Incroporating Single Crystal Plasticity in the ABAQUS Finite Element Program, Harvard Univ., 1991.

[59] G. K. Sfantos, M. H. Aliabadi, A boundary cohesive grain element formulation for modelling intergranular microfracture in polycrystalline brittle materials, International Journal for Numerical Methods in Engineering 69 (2007) 1590–1626.

[60] G. K. Sfantos, M. H. Aliabadi, Multi-scale boundary element modelling of material degradation and fracture, Computer Methods in Applied Mechanics and Engineering 196 (2007) 1310–1329.

[61] A. Kuzmin, M. Luisier, O. Schenk, Fast methods for computing selected elements of the greens function in massively parallel nanoelectronic device simulations, in: F. Wolf, B. Mohr, D. Mey (Eds.), Euro-Par 2013 Parallel Processing, Vol. 8097 of Lecture Notes in Computer Science, Springer Berlin Heidelberg, 2013, pp. 533–544.

[62] O. Schenk, M. Bollhöfer, R. A. Römer, On large-scale diagonalization techniques for the anderson model of localization, SIAM Rev. 50 (1) (2008) 91–112.

[63] O. Schenk, A. Wchter, M. Hagemann, Matching-based preprocessing algorithms to the solution of saddle-point problems in large-scale nonconvex interior-point optimization, Computational Optimization and Applications 36 (2-3) (2007) 321–341.

[64] I. Benedetti, M. H. Aliabadi, G. Davì, A fast 3D dual boundary element method based on hierarchical matrices, International Journal of Solids & Structures 45 (2008) 2355–2376.

[65] I. Benedetti, A. Milazzo, M. H. Aliabadi, A fast dual boundary element method for 3D anisotropic crack problems, International Journal for Numerical Methods in Engineering 80 (2009) 1356–1378.

[66] T.-Y. Wu, J. L. Bassani, C. Laird, Latent hardening in single crystals i. theory and experiments, Proceedings of the Royal Society of London A: Mathematical, Physical and Engineering Sciences 435 (1893) (1991) 1–19.

[67] E. Lutz, W. Ye, S. Mukherjee, Elimination of rigid body modes from discretized boundary integral equations, International Journal of Solids and Structures 35 (33) (1998) 4427–4436.

[68] R. Quey, P. R. Dawson, F. Barbe, Large scale 3D random polycrystals for the finite element method: Generation, meshing and remeshing, Computer Methods in Applied Mechanics and Engineering 200 (2011) 1729–1745.

[69] Z. Hashin, S. Shtrikman, A variational approach to the theory of the elastic behaviour of polycrystals, Journal of the Mechanics and Physics of Solids 10 (4) (1962) 343–352.

[70] M. Berveiller, A. Zaoui, An extension of the self-consistent scheme to plastically-flowing polycrystals, Journal of the Mechanics and Physics of Solids 26 (5) (1978) 325–344.

[71] L. Méric, G. Cailletaud, Single crystal modeling for structural calculations: Part 2finite element implementation, Journal of Engineering Materials and Technology 113 (1) (1991) 171–182.

[72] C. Gérard, G. Cailletaud, B. Bacroix, Modeling of latent hardening produced by complex loading paths in fcc alloys, International Journal of Plasticity 42 (2013) 194–212.

[73] B. Devincre, L. Kubin, T. Hoc, Physical analyses of crystal plasticity by dd simulations, Scripta Materialia 54 (5) (2006) 741–746.

[74] R. A. Lebensohn, A. K. Kanjarla, P. Eisenlohr, An elasto-viscoplastic formulation based on fast fourier transforms for the prediction of micromechanical fields in polycrystalline materials, International Journal of Plasticity 32 (2012) 59–69.

[75] Y. Liu, Fast multipole boundary element method: theory and applications in engineering, Cambridge university press, 2009.

[76] M. Bebendorf, Hierarchical matrices, Springer, 2008.

[77] I. Benedetti, M. Aliabadi, A fast hierarchical dual boundary element method for three-dimensional elastodynamic crack problems, International journal for numerical methods in engineering 84 (9) (2010) 1038–1067.

52

[78] A. Milazzo, I. Benedetti, M. Aliabadi, Hierarchical fast bem for anisotropic time-harmonic 3-d elastodynamics, Computers & Structures 96 (2012) 9–24.

[79] C. Miehe, J. Schröder, J. Schotte, Computational homogenization analysis in finite plasticity simulation of texture development in polycrystalline materials, Computer methods in applied mechanics and engineering 171 (3) (1999) 387–418.

[80] M. B. Bettaieb, O. Débordes, A. Dogui, L. Duchêne, C. Keller, On the numerical integration of rate independent single crystal behavior at large strain, International Journal of Plasticity 32 (2012) 184–217.

[81] I. Simonovski, L. Cizelj, Automatic parallel generation of finite element meshes for complex spatial struct Computational Materials Science 50 (5) (2011) 1606 – 1618. doi:10.1016/j.commatsci.2010.12.014.
URL http://www.sciencedirect.com/science/article/pii/S0927025610006713

[82] I. Simonovski, L. Cizelj, Towards modeling intergranular stress corrosion cracks on grain size scales, Nuclear Engineering and Design 246 (0) (2012) 107 – 114.

Highlights for the manuscript
A grain boundary formulation for crystal plasticity
by
I. Benedetti, V. Gulizzi, V. Mallardo

- The first boundary element formulation for crystal plasticity is presented
- The formulation is valid for 3D small strains crystal plasticity problems
- Both single crystal as well as polycrystalline problems are considered
- The polycrystalline problem is formulated in terms of inter-granular variables only
- The method allows a reduction of DoFs, appealing for multiscale analysis